POLITECNICO DI MILANO

School of Industrial and Information Engineering

Department of Electronics, Information and Bioengineering

Master of Science in Biomedical Engineering

Towards deformable registration for augmented reality in robotic assisted partial nephrectomy

Supervisor: Elena DE MOMI, PhD

Co-supervisor: Dott. Ing. Sara MOCCIA

Author:

Anna MORELLI, ID: 853814

Academic Year 2016-2017

Abstract

Kidney tumor is the twelfth most common type of cancer, with 338,000 new cases annually diagnosed. The most effective treatment for small tumors is the surgical resection of the tumoral tissue. The treatment procedure is called partial nephrectomy.

Partial nephrectomy can be performed in Minimaly Invasive Surgery (MIS), whose advantages for the patient, when compared to open surgery, are bleeding reduction, smaller incision size, less pain, shorter recovery time and lower risk of infection. The main MIS disadvantages are, for the surgeon, the loss of depth perception and the difficulty in intra-operative identification of relevant anatomical structures. In the last years, Robotic MIS (RMIS) has become spread; the advantages are 3D view, tremor filtering and wide surgical instrument range of motion. However, RMIS suffers from the same drawback of MIS.

A solution to overcome these drawbacks is provided by Augmented Reality (AR). AR refers to the superimposition on the intra-operative scene of virtual elements, such as the patient-specific anatomical model. AR can help providing intra-operative guidance, information matching and identification of the relevant structures.

Integrating AR in partial nephrectomy requires to deal with intra-operative organ deformation in 3D (due to insufflation, organ manipulations and changes in position), that is still an open issue. The hypothesis of this thesis is that exploiting deformable registration is crucial to tackle intra-operative tissue deformation.

The focus of this work is on the registration between the pre-operative kidney model and the intra-operative kidney surface.

The patient-specific kidney pre-operative model was obtained from pre-operative Computed Tomography (CT). The CT was segmented with a semiautomatic method exploiting deformable active contour models. From the obtained segmentation mask, the kidney model was retrieved. The model vertexes were retrieved in order to perform a surface-based registration.

The intra-operative kidney images were acquired with the da Vinci Research Kit stereocamera. Kidney surface was reconstructed with a dense soft-tissue 3D reconstruction. The intra-operative kidney surface was retrieved as point cloud.

Intra-operative registration was then performed between the pre-operative model and the intra-operative point cloud in two steps: (i) intial alignment was performed manually or with pair-point matching algorithm based on corresponding markers (manually identified by an user), (ii) deformable registration refining was performed with Free Form Deformation (FFD) algorithm based on B-splines.

For experimental purpose, a kidney silicon phantom was developed according to the patient-specific model in order to acquire the intra-operative point cloud.

The registration algorithms were implemented in C++ using the Visualization Toolkit (VTK) and the Insight Segmentation and Registration Toolkit (ITK) libraries.

To test the registration workflow in a controlled environment, an intra-operative point cloud was manually created deforming the kidney model. The registration gave high results when registering in 2D the kidney model boundary to the kidney deformed boundary with different levels of deformation (mean Root Mean Square Error (RMSE) reduction ($-\Delta_{RMSE}$) was 34.68%). The results were good when the registration was performed in 3D (mean $-\Delta_{RMSE}$ was 6.27%). The relation between the algorithm performance and the deformation level was statistically investigated with the Wilcoxom signed-rank test ($\alpha = 0.05$) showing that the algorithm was robust with respect to the deformation level.

In both the cases, the performance of FFD were significantly higher (Wilcoxon signed-rank test, $\alpha = 0.05$) compared to a rigid registration algorithm.

The developed workflow was tested to register the 3D kidney model to the intra-operative point cloud acquired on phantom. The best $-\Delta_{RMSE}$ obtained in the (i) initial alignment was 89%. The best $-\Delta_{RMSE}$ obtained in the (ii) deformable registration was 28%. The overall registration process best $-\Delta_{RMSE}$ was 91%.

The high $-\Delta_{RMSE}$ highlights the need, in a partial nephrectomy AR system, to tackle the intra-operative kidney deformation with deformable registration algorithm.

Sommario

Il tumore al rene é il dodicesimo tipo di cancro piú comune in entrambi i sessi, con 338 000 nuovi casi ogni anno. Il trattamento piú efficace per tumori di piccola taglia é la rimozione chirurgica del tessuto tumorale. La procedura é chiamata nefrectomia parziale.

La nefrectomia parziale si puó eseguire in chirurgia microinvasiva, i cui vantaggi per il paziente, rispetto all'esecuzione in chirurgia aperta, sono minore sanguinamento, meno dolore, tempo di ricovero piú breve e minor rischio di infezioni. I maggiori svantaggi della chirurgia microinvasiva sono, dal punto di vista del chirurgo, la perdita della percezione della profonditá e la difficoltá nell'identificare le strutture anatomiche di interesse durante la procedura.

Negli ultimi anni, l'uso di sistemi robotici nella chirurgia microinvasiva si é diffuso; i vantaggi sono la visione 3D, il filtraggio del tremore e una migliore mobilitá degli strumenti chirurgici. Tuttavia, la chirugia robotica microinvasiva ha le stesse limitazioni in termini di perdita di profonditá e difficoltá nell'identificazione delle strutture. Una soluzione a queste problematiche é offerta dalla realtá aumentata. La realtá aumentata consiste nella sovrapposizione sulla scena intraoperatoria di elementi virtuali, ad esempio il modello anatomico specifico per il paziente. La realtá aumentata puó offrire supporto fornendo una guida nel contesto intraoperatorio, permettendo la fusione delle informazioni e lidentificazione delle strutture di interesse.

Per l'integrazione della realtá aumentata nella nefrectomia parziale, un problema tuttora aperto riguarda il trattamento della deformazione intraoperatoria degli organi, dovuta all'insufflazione del paziente, alla manipolazione degli organi e ai cambi di posizione. L'ipotesi su cui si basa questa tesi é che utilizzare la registrazione deformabile é cruciale per trattare la deformazione intraoperatoria dei tessuti.

Il punto centrale di questo lavoro é la registrazione tra il modello preoperatorio del rene e la sua superficie visibile intraoperativamente.

Il modello preoperatorio del rene del paziente é stato ottenuto da una tomografia computerizzata eseguita preoperativamente e segmentata con un metodo semiautomatico che utilizza deformable active contour model. Il modello del rene é stato poi ricavato utilizzando l'algoritmo di fast marching method. I vertici del modello sono stati estratti per poter eseguire una registrazione basata sulla superficie.

Le immagini intraoperatorie del rene sono state acquisite con la stereo camera del da Vinci Research Kit. La superficie del rene é stata ricavata con una ricostruzione 3D densa dei tessuti molli e la nuvola di punti é stata ottenuta.

La registrazione intraoperatoria é stata poi eseguita tra il modello preoperatorio e la nuvola di punti intraoperatoria in due step: (i) l'allineamento iniziale é stato eseguito manualmente o con un algoritmo basato su punti corrispondenti (che devono essere identificati manualmente), (ii) l'aggiustamento é stato eseguito con un algoritmo di registrazione deformabile Free Form Deformation (FFD), basato su B-splines.

Per ragioni sperimentali, un fantoccio di silicone del rene é stato sviluppato secondo il modello specifico del paziente per acquisire la nuvola di punti intraoperatoria.

Gli algoritmi di registrazione sono stati implementati in C++ utilizzando le librerie Visualization Toolkit (VTK) e Insight Segmentation and Registration Toolkit (ITK).

Per testare il sistema in un ambiente controllato, una nuvola di punti intraoperatoria é stata creata deformando manualmente il modello del rene. I risultati della registrazione mostravano che si otteneva un'alta accuratezza registrando in 2D i contorni del modello del rene sui contorni del rene deformato (la riduzione $-\Delta_{RMSE}$ media del Root Mean Square Error (RMSE) era del 34.68%) testando diversi livelli di deformazione. I risultati sono stati buoni quando la registrazione é stata eseguita in 3D (il $-\Delta_{RMSE}$ era del 6.27%). Il legame tra i risultati dell'algoritmo e il livello di deformazione é stato investigato statisticamente con il test di Wilcoxon ($\alpha = 0.05$) mostrando che l'algoritmo é robusto rispetto alla deformazione.

In entrambi i casi, i risultati di FFD erano significativamente (test di Wilcoxon con $\alpha = 0.05$) piú alti di quelli ottenuti con un algoritmo di registrazione rigido.

L'algoritmo di registrazione é stato utilizzato per registrare il modello 3D del rene alla nuvola di punti intraoperatoria acquisita sul fantoccio. Il miglior $-\Delta_{RMSE}$ ottenuto (i) nell'allineamento iniziale é stato del 89%. Il miglior $-\Delta_{RMSE}$ ottenuto (ii) nella fase

di registrazione deformabile é stato del 28%. Il miglior $-\Delta_{RMSE}$ calcolato su entrambi gli step é stato del 91%.

Gli alti $-\Delta_{RMSE}$ ottenuti evidenziano la necessitá, in un sistema che utilizza realtá aumentata in nefrectomia, di trattare la deformazione intraoperatoria del rene con algoritmi di registrazione deformabile.

Contents

1 INTRODUCTION **1**

1.1 Nephrectomy 3

1.1.1 Nephrectomy in MIS 3

1.1.2 Robotic MIS 4

1.2 Augmented reality 5

1.2.1 Pioneering AR systems in MIS 6

1.2.2 AR systems in nephrectomy 8

1.2.3 Limits in the AR systems in nephrectomy 9

1.3 Aim of the thesis 11

2 LITERATURE REVIEW **13**

2.1 Registration 13

2.1.1 Rigid registration 14

2.1.2 Deformable registration 15

2.2 Registration approaches 16

2.2.1 Manual approach 16

2.2.2 Point-based approach 17

2.2.3 Surface-based approach 19

2.2.4 Volume-based approach 19

2.3 Limits in the registration literature for AR in nephrectomy 21

3 MATERIALS AND METHODS **23**

3.1 Methods 23

3.1.1 Model generation 24

3.1.2 Calibration and 3D reconstruction 24

3.1.3 Registration 25
3.1.3.1 Initial alignment 25
3.1.3.2 Deformable registration 27
3.1.4 Phantom development 29
3.1.5 Implementation 30
3.2 Materials 30
3.3 Evaluation protocol 32
3.3.1 E1: investigation of n_x and n_y 33
3.3.2 E2: trade-off between number of iteration and $-\Delta_{RMSE}$ 33
3.3.3 E3: Comparison between FFD and ICP in 2D 33
3.3.4 E4: Comparison between FFD and ICP in 3D 34
3.3.5 E5: Registration of $M1$ to $F2$ with manual initial alignment . . 34
3.3.6 E6: Registration of $M2$ to $F2$ with manual initial alignment . . 34
3.3.7 E7: Registration of $M1$ to $F2$ with point-based initial alignment 34
3.3.8 E8: Registration of $M2$ to $F2$ with point-based initial alignment 35

4 RESULTS **37**

5 DISCUSSION **49**

6 CONCLUSIONS AND FUTURE WORK **53**

Bibliography **65**

Chapter 1

INTRODUCTION

Kidney tumor is the 12th most common type of cancer [1], with 338,000 new cases annually diagnosed[1]. Men are more affected by kidney tumor[2], as shown in Fig. 1.1. The occurrence is higher, both for male and female, in the developed regions with respect to the developing ones, considering the estimated age-standardized rates.

Risk factors for kidney tumors are smoking, obesity, high blood pressure and exposure to carcinogenic arsenic[3]. Moreover, some chemicals as asbestos, cadmium, some organic solvents, pesticides and fungal toxins and some steroidal estrogens are suspected to be risk factors for kidney tumor. Another risk factor is the presence of kidney

[1]https://www.worldatlas.com/articles/countries-with-the-highest-incidenceof-kidney-cancer-in-the-world.html

[2]http://www.wcrf.org/int/cancer-facts-figures/worldwide-data

[3]https://www.cancer.org/cancer/kidney-cancer/causes-risks-prevention/risk-factors.html

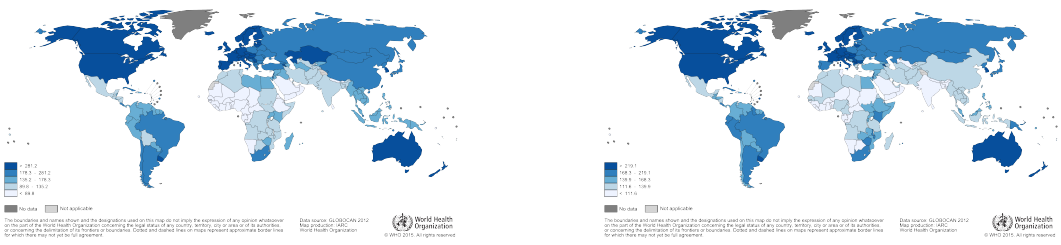

(a) *Incidence for Men.* **(b)** *Incidence for Women.*

Figura 1.1: *Estimated cancer incidence worldwide in 2012 according to WHO.*

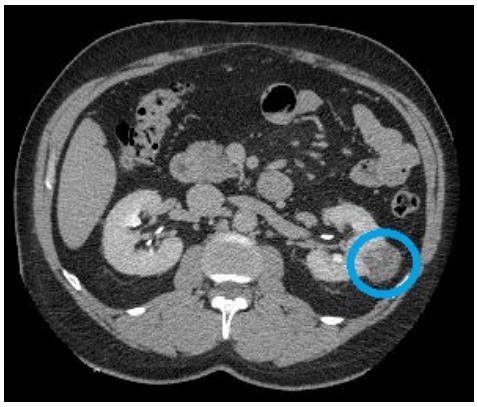

Figura 1.2: *Kidney cancer in computed tomography.*

diseases such as the von Hippel-Lindau disease, the Birt-Hogg-Dube syndrome, Cowden syndrome and Tuberous sclerosis and genetic factors.

An example of kidney cancer seen in a Computed Tomography (CT) in shown in Fig. 1.2. Treatment options for kidney tumor include [4]:

- Surgery: surgical treatment (nephrectomy) is the most effective choice for several type of kidney cancers. It assures the best treatment outcomes for the patient.

- Ablation: for people who cannot undergo surgery, ablation is a treatment option. Ablation treatments include cryotherapy, radiofrequency ablation and arterial embolization.

- Radiation therapy: high-energy radiation are used to treat cancer cells. However, kidney cancer cells are not very sensitive to radiation, so this treatment is not common.

- Targeted therapies: used to treat advanced cancer or as complementary therapy after surgery. The target therapies block angiogenesis (growth of the new blood vessels that nourish cancers) or important proteins in cancer cells necessary for their lives.

- Chemotherapy. The treatment is rarely used since kidney tumor is really resistant to chemo drugs.

[4] http://pubs.rsna.org/doi/full/10.1148/rg.266065010

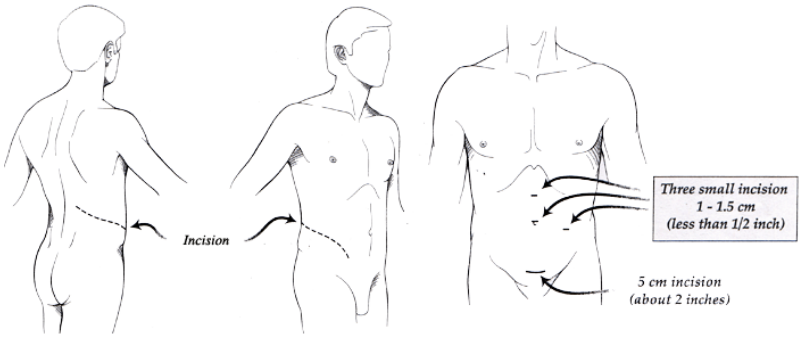

Figura 1.3: *Ports comparison in open (left) and laparoscopic surgery (right).*

In Sec. 1.1 nephrectomy is discussed in detail, as it represents the main treatment option.

1.1 Nephrectomy

There are three main kinds of nephrectomy:

- Simple nephrectomy: the entire kidney affected by tumor is removed.
- Radical nephrectomy: the surgeon removes the entire kidney, the layer of fat surrounding the kidney, the ureter, the adrenal gland and nearby lymph nodes.
- Partial nephrectomy: only tumoral tissue is removed, preserving healthy tissues.

In the last decades, all kinds of nephrectomy were traditionally performed in open surgery. Through the aperture in the abdomen, open surgery allows the surgeon to direct access the healthy tissues and the tumor and to identify them clearly according to their appearance, texture and consistency.

However, it presents several drawbacks for the patients, such as high bleeding, long recovery time, pain and high risk of infection. To overcome such drawbacks, Minimal Invasive Surgery (MIS) has recently become a valid alternative to open surgery.

1.1.1 Nephrectomy in MIS

Nowadays, laparoscopic partial nephrectomy, i.e. performed in MIS, is considered to be the standard of care for small renal tumors [2]. In MIS procedures, three or four

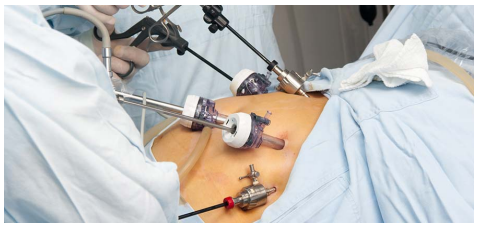

Figura 1.4: *Set-up in laparoscopic nephrectomy.*

incisions are made in the patient's abdomen to provide access for surgical instruments and endoscope. Differences incision size for open nephrectomy and laparoscopic nephrectomy are shown in Fig. 1.3.

MIS leads to proved benefits for the patient such as reduction of bleeding, recovery time, scar dimension, pain and risk of infection [3, 4].

In MIS nephrectomy, the kidney and eventually the surrounding structures are detached internally, placed in an impermeable bag and removed through one of the incisions using a morcellator. The procedure set-up is shown in Fig. 1.4.

1.1.2 Robotic MIS

In the last years, Robotic MIS (RMIS) has become more and more spread. The birth of the RMIS can be set in the '90s, even if robots where used in surgery since '80s [5]. Ones of the first robotic devices for MIS in neurosurgery were developed in [6] and [7]. In the next years, some robotic devices for MIS were developed and commercialized, for example NeuroMate and NeuroArm in the neurosurgery field and da Vinci in the laparoscopic field.

Nowadays, robotic systems for RMIS provide three-dimensional view, tremor filtering and allow for a wide range of motion of the surgical instruments.

However, both MIS and RMIS present some criticisms, such as the impairment of haptic feedback for detailed discrimination of different structures, the loss of depth perception due to the monocular endoscopic camera and the surgeon disorientation. The lack of haptic feedback can be partially solved introducing force feedback in the instruments, to improve the quality and safety of the surgical procedure [8].

To overcome these drawbacks, Image Guided Surgery (IGS) or computer integrated surgery has progressively become more popular. The IGS aim is to integrate the

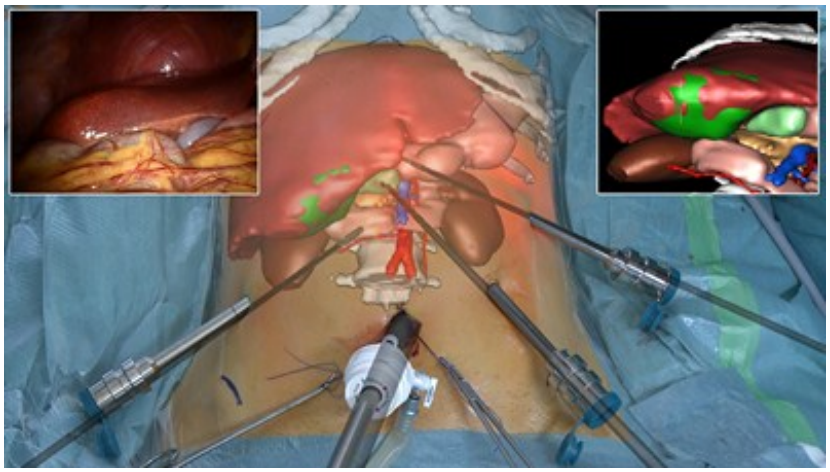

Figura 1.5: *Augmented reality in surgery. On the intra-operative scene organs model are projected (central). The endoscopic view is displayed without augmentation (left) and with augmentation (right).*

computer technologies to the surgical procedures [9]. IGS can integrate intra-operative imaging system to identify, in the Operating Room (OR), the trajectories and the relevant structures identified in the pre-operative phase, or can use pre-operative images to retrieve patient-specific anatomical model. Thus, it provides navigational aid [10]. Among IGS methodologies, Augmented Reality (AR) has several applications in laparoscopic nephrectomy.

1.2 Augmented reality

AR is the superimposition and combination on a real view (the intra-operative scene) of some virtual elements (the patient-specific anatomy) not visible in that view [11, 8] and reported on a screen, as is shown in Fig. 1.5. Moreover, sensitive structures, such as vessels, can be identified in the pre-operative plan [12] and their intra-operative position can be retrieved with AR systems. The robot can be avoided to enter such forbidden structures, e.g. with the implementation of Active-Constraints (AC) control. The patient-specific anatomy is obtained with high resolution anatomical imaging, such as CT or Magnetic Resonance Imaging (MRI). The anatomy can be acquired both in the pre-operative (more common) on in the intra-operative phase. The intra-operative view is often the endoscopic view.

The proved benefits of AR are, as reported in [13]:

- Intra-operative guidance is provided with rapid identification of targets and critical structures.
- The match of the information from different sources is made by the system, so the surgeon's cognitive load is reduced since and the procedure efficiency is increased.
- The pre-operative plan can be represented in the intra-operative scene.
- Surgeon's disorientation due to the narrow laparoscopic field of view is avoid.

During nephrectomy, AR environment offers a potential clinical advantages in two stages [14]:

1. In the initial phase of the procedure, identifying important structures such as the major vessels and the renal vessels.
2. During tumor resection, fixing negative surgical margins that the instruments can not pass. In this case, the accuracy of the augmentation is a critical parameters and should assure resection margin of 5-7 mm [14, 15, 16].

The application of AR in case of soft tissues, as in the abdominal cavity, presents a big challenge: intra-abdominal organs and, even more so, the kidneys are deformable and not constant in their relationship with the anatomical landmarks surrounding them. The changes are due to high pressure (the patient is insufflated during the procedure), to different patient's position, to growth or reduction of tumor, to renal vessels clamping and to the surgeon organs manipulation and dissection. To overcome those errors in the superimposition of the anatomy to the scene, the deformations of the pre-operative anatomy should be taken into account.

1.2.1 Pioneering AR systems in MIS

The first documented AR systems trials are performed in the neurosurgery field; the reason is the presence of the skull, a rigid structure presents both in pre-operative phase and in the intra-operative one, allowing the superimposition of frames of the two phases

according to the stereotactive approach. Stereotaxis is a branch of surgery which entails the 3D localization of the target expressed with respect to rigid frame solid with the patient. The brain shift, i.e. the brain deformation occurring when the skull is open, is very limited (but still present) and usually is assumed null. Thus, it is relatively easy to superimpose pre-operative and intra-operative data under the assumption of rigidity. An example of superimposition of the anatomy to the intra-operative scene is reported in Fig. 1.6.

The AR appears in the '80s: Roberts and his team [17] superimpose tumor boundaries obtained from CT to the microscope view in the OR. The superimposition is made possible by the intra-operative localization of the microscope using Ultra Sounds (US) to determine position and orientation of the probe.

In the same years, Kelly et al. [18] superimpose the anatomy extracted from pre-operative CT to the stereotaxic space. The result is used to guide the laser resection of the tumor, guaranteeing control to avoid healthy regions.

In the '90s, studies speculate on the application of AR in tumor treatment in the neurosurgical field, such as [19]. Another AR application investigated is in the bypass

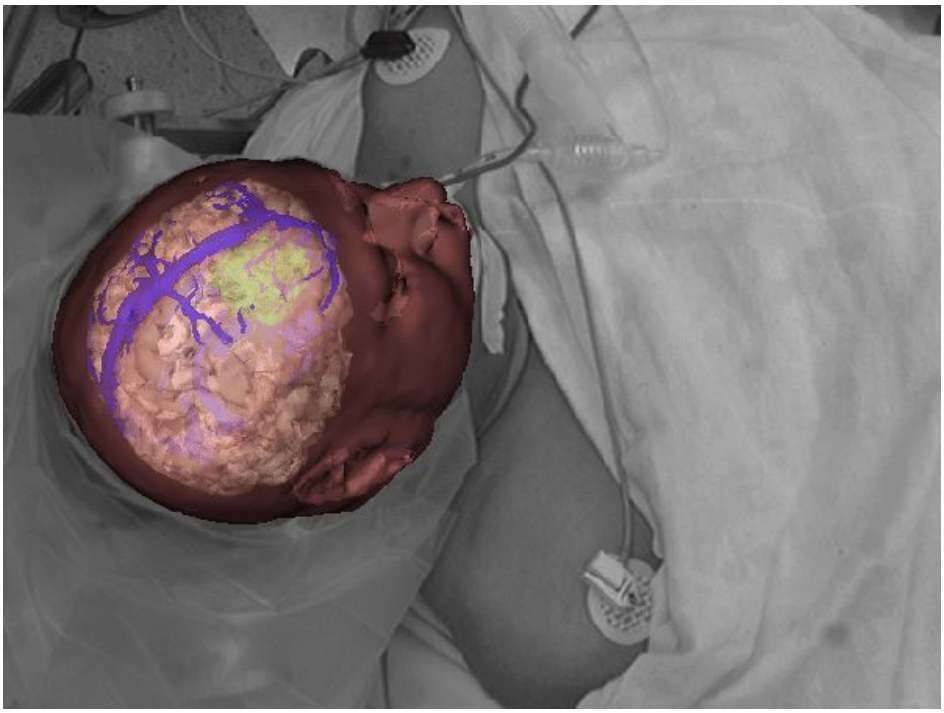

Figura 1.6: *Augmented reality in neurosurgery.*

Figura 1.7: *Augmented reality in nephrectomy: superimposition of the intra-operative anatomy to the intra-operative scene. From [30].*

surgery, as is shown by Cabrilo et al. [20]. Thanks to the big amount of studies and works on this topic [21, 22, 23], nowadays AR in neurosurgery is the standard [13]. In other filed such as otolaryngology, maxillofacial surgery, opthalmology, orthopedics and dental surgery system integrating AR are used.

In the procedures in which there are not rigid supporting structures like bones, the AR is not the standard and presents big challenges, because the tissue deformation is still an open issue. One of the first trials to apply the AR on deformable tissues is made by [24], where the anatomy extracted from US is projected, through a display, on the abdomen of a pregnant woman. In general surgery, an application is in [25]. The first AR systems used in laparoscopy are [26] for pancreatico-duodenectomy, [27] for liver segmentectomy, [28] for laparoscopy and [29] for urology.

1.2.2 AR systems in nephrectomy

An overview about the AR systems developed for the partial nephrectomy is reported in [14]. In [31, 32, 33, 34] the pre-operative kidney anatomy is rigidly superimposed to the intra-operative scene: the hypothesis is the presence of small and negligible

intra-operative deformation.

One diffused approach is the superimposition of a 3D anatomy extracted intra-operatively (from MRI, cone-beam CT or US) to the intra-operative scene, as in [30, 35, 36, 37, 38], whose result is shown in Fig 1.7. Since the intra-operative anatomy has exactly the same shape seen in the endoscope, the errors due to the deformation of the kidney are null. In most of these works, the use of optical or magnetic tracker is necessary to determine the spatial transformation necessary to superimpose the images. However, exploiting intra-operative imaging requires CT or MRI equipped OR and, in case of CT, further radiation dose is delivered to the patient.

Another approach is the deformation of the pre-operative anatomy with biomechanical model to overcome the issue of intra-operative deformation. In [10, 39] the superimposition with rigid methods is coupled with deformation of the pre-operative anatomy. In the first, the effects of clamping and incision are considered, while in the second the effects of loss of perfusion and changes in pressure. The limit of this approach is the requirement of complex models to be compute.

An innovative solution is proposed in [40]: a pre-operative anatomy extracted from CT is superimposed to the intra-operative images by means of deformable algorithm. The main advantages are the avoidance, to deform the kidney anatomy, of biomechanical models, made possible by the use of deformable registration algorithm.The registration error observed is < 1 mm and uncertainties are projected on a single crisp contour. The AR visualization is limited to the boundaries (2D) of the relevant structures, not to the entire volume.

1.2.3 Limits in the AR systems in nephrectomy

The existing AR systems in nephrectomy, as reported in Sec. 1.2.2, highlights some limits in tackling organ deformations occurring in the OR. Lots of methods do not tackle the organ deformation occurring in the intra-operative scenario and rely on rigid sovrapposition of the pre-operative model to the intra-operative scene. These methods are based on the hypothesis that the augmentation obtained in that way is sufficient accurate. However, in a real OR the kidney and all the abdominal organs undergo a deformation that can not be considered null.

Other methods require an additional imaging system inside the OR, however to have an OR equipped with MRI or CT is expensive, it is challenging and, in case of CT, require to deliver to the patient an extra dose of radiation.

The use of biomechanical model to model the intra-operative deformation on the kidney model are affected by the limitation of high number of parameters to be computed, so are not do used.

There is only one case in which the registration between the pre-operative model and the intra-operative endoscopic images is performed with deformable registration algorithm [40]. However, the augmentation of the scene in limited to the 2D tumor boundary and no information about the rest of the model is displayed on the screen. This is useful to support the localization of the tumor, but it can not be considered a AR system able to represent the high resolution pre-operative model on the intra-operative scene. It neglects all the knowledge about the kidney model.

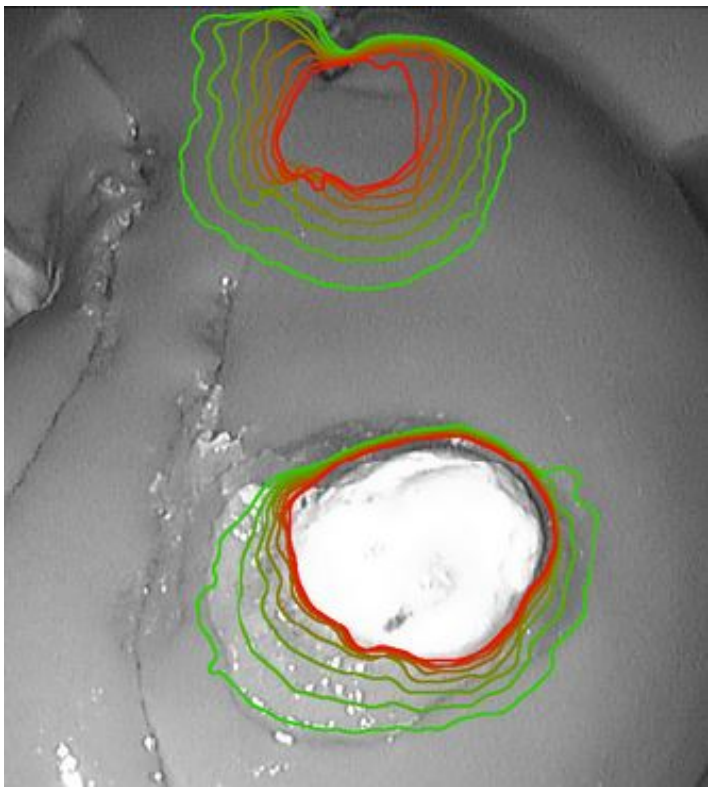

Figura 1.8: *From [40]. 2D tumor boundaries extracted from pre-operative CT are projected onto the intra-operative endoscopic images. Each contour has associated a probability.*

1.3 Aim of the thesis

The aim of this thesis is to investigate the use of a deformable registration algorithm to register the 3D kidney model to the 3D intra-operative endoscopic scene. This is done towards the use of an AR system to support the surgeon while performing laparoscopic nephrectomy.

The problem of the 3D intra-operative kidney deformation will be tackled with deformable registration algorithms. The deformable registration algorithm used was Free Form Deformation (FFD) based on B-splines. First, it was used to register the 3D model to manually created intra-oerative point cloud, to obtain the results in terms of registration accuracy in a controlled environment and with a defined level of deformation; the results were compared also to evaluate if the algorithm is robust to tackle different levels of deformation. Secondly, it was used to register the model extract from real CT to a point cloud retrieved with the da Vinci Research Kit (dVRK)[5] stereocamera (720x576 pixels, 25 Hz, 80 degrees field of view) and acquired on silicon kidney phantom obtained according to the model.

[5]http://research.intusurg.com/dvrkwiki

Chapter 2

LITERATURE REVIEW

In this Chapter, the registration process involved in AR system for partial nephrectomy will be described.

The approach can be split in two phases, according to [13]. The first phase is the initial registration. In this phase, the organ anatomy is aligned with the intra-operative view, usually endoscopic images: an high accuracy should be achieved in this phase. The organ anatomy can be extracted from pre-operative or intra-operative imaging systems; the most used imaging systems to retrieve the patient-specific organ 3D model are MRI and CT, due to their high resolution.

The second phase is tracking: the aim is to maintain the accurate augmentation obtained with the initial registration during the entire procedure. Tracking is not described into details since it is not the aim of this thesis, the reader can refer to [13, 41] for more information.

2.1 Registration

Registration is the process by which the transformation necessary to superimpose a given dataset to another one is found, such that the spatial locations of the corresponding points coincide [42].The transformation is the mathematical operators that maps one dataset into another one.

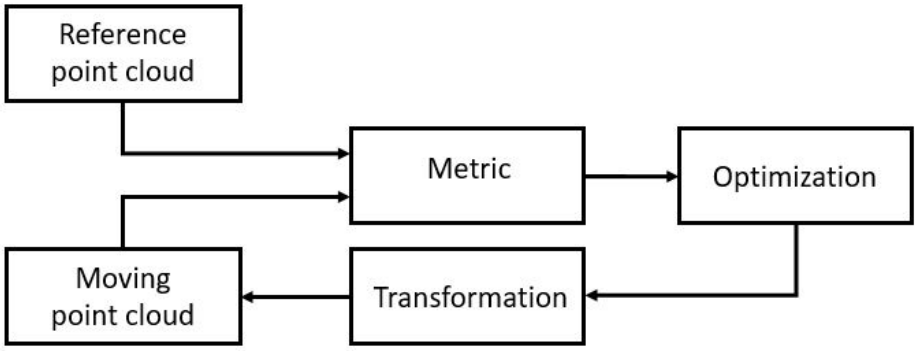

Figura 2.1: *The registration workflow to register the moving point cloud to the reference point cloud. A metric based on distance is set between the two point clouds. The metric is optimized for finding the best parameters to be used in the transformation (i.e. the mathematical operators that maps one dataset into another one). The transformation is applied to the moving point cloud. This process is iteratively done until convergence in terms of metric reduction is reached.*

Registration can be applied both to images or to point clouds. The registration in this work is applied to point clouds, so only approaches referred to them are reported.

The general workflow of the registration process is represented in Fig. 2.1. A metric is set to describe the differences or the distance between a point cloud used as reference and a point cloud that has to be registered (moving point cloud). This metric has to be optimized, so the point clouds are forced to be as closer as possible. The parameters obtained with the optimization process are used to update the transformation. The transformation is then applied to the moving point cloud and, if the disparity between the two point clouds is below a fixed value, the registration is gained, otherwise the cycle is repeated until a convergence is reached.

In an AR system for nephrectomy, the registration involves the superimposition of the kidney model (from which the moving point cloud is obtained) to the intra-operative view (from which the reference point cloud is retrieved). The registration can be rigid or deformable.

2.1.1 Rigid registration

The transformation is described by six degree of freedom in 3D, three for rotation and three for translation (rototranslation). The underlying hypothesis is the rigidity of the structures. The most used rigid registration algorithm is Iterative Closest Point (ICP).

ICP is described in [43, 44] and it is the most used thanks to its simplicity and low complexity. The algorithm iteratively:

- Assigns correspondences between each point of the moving point cloud $\vec{m} \in M$ to the closest point of the reference point cloud $\vec{f} \in F$. The minimum of the Euclidean distance ($d(\vec{m}, F)$) is used to set the correspondence:

$$d(\vec{m}, F) = \min_{f \in F} \|\vec{m} - \vec{f}\| \tag{2.1}$$

  For the entire M, the correspondence relation (Y) can be computed:

$$Y = \mathcal{C}(M, F)$$

- Computes the registration parameters: a cost function based on the Euclidean distance between corresponding points is optimized ($d(M, F)$):

$$d(M, F) = \sum_{\vec{m} \in M} \min_{\vec{f} \in F} \|\vec{f} - \vec{m}\| \tag{2.2}$$

  The quaternion representation of the rotation $\vec{q_R}$ and of the translation $\vec{q_T}$ is retrieved.

- Applies the obtained registration to the moving dataset M.

until convergence is reached with a certain tolerance. In AR system for partial nephrectomy ICP is used in [31, 32, 33, 10, 30, 38].

2.1.2 Deformable registration

The transformation is described by from six up to infinite degree of freedom, since the deformation model can be selected as complex as desired. A completed overview of the deformable registration method used in the medical field is reported in [45].

One possible transformation is Vector Field (VF). VF is a grid in which each block has associated a displacement vector, representing the direction and the intensity applied to what is inside that block, as shown in Fig. 2.2. To find the optimal parameters to describe the displacement vectors, a cost function, based on the similarity of the two point sets and on some smoothness criteria, has to be minimized. The most used algorithms to compute VF parameters are:

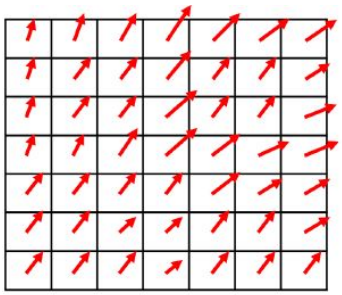

Figura 2.2: *The Vector Field (VF) is a possible transformation involved in registration. VF is a grid superimposed to the point cloud, in which each block has associated a displacement vector, representing the direction and the intensity applied to what is inside that block.*

- Thin-plate spline: it requires corresponding markers and it is based on the minimization of their corresponding distance.

- Non-rigid FFD based on B-spline: used when there are not corresponding markers in the point clouds [46, 47]. To compute the similarity, a measure of the distance between the two sets is used. FFD is a deformation model based on the interpolation theory [45].

Once the VF is computed, it is applied to the moving point cloud.

2.2 Registration approaches

Disregarding the type of transformation used, it is possible to identify different approaches according to the set-up and to the available data.

2.2.1 Manual approach

The registration between the kidney model and the intra-operative endoscopic images is performed by an expert and relies on manual input. The manual approach can perform both rigid and non-rigid registration.

In nephrectomy, this approach is used in [36] to rigidly align the kidney model extracted from intra-operative CT to the endoscopic images. This strategy can be also used integrated with other strategies, for example to initialize surface-based (Sec. 2.2.3) as in [40] or volume-based approaches (Sec. 2.2.4) or for a final refinement as in

[34]. In this paper, the manual registration perform by surgeon in the OR is used to adjust the rigid registration of the pre-operative kidney model to the intra-operative images; the first step of the registration is computed with a point-based approach (Sec. 2.2.2).

2.2.2 Point-based approach

In the point-based approach (Fig. 2.3) the registration is performed between two sets of corresponding points, one from the moving point cloud, one from the fixed one. So, it is necessary to have anatomical landmark or artificial markers (usually stuck to the organ and acquired with the help of tracking system) visible both in the kidney model and in the intra-operative images. Considering abdominal procedures, no rigid landmarks are available and fiducial points have to be retrieved intra-operatively exploring the scene. The markers are usually rigidly aligned.

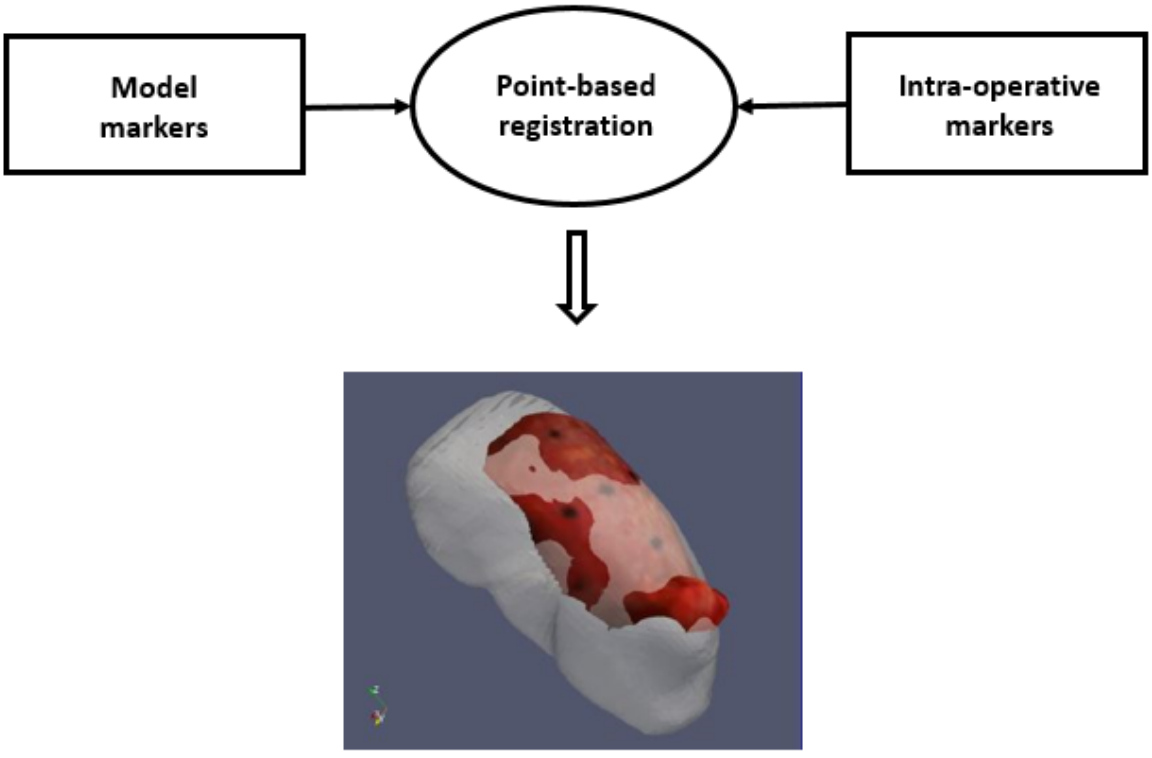

Figura 2.3: *The point-based approach: the registration is performed between markers (black dots) from the model (gray) and markers from the intra-operative endoscopic image (red). The result is from [31].*

In nephrectomy, the point-based approach is used in [39] to register the model obtained from high resolution pre-operative CT, deformed with a biomechanial model to take into account loss of perfusion and pressure, to the model obtained from low resolution intra-operative CT; the used markers are spheres sutured onto the surface. However, the use of the point-based approach is most common as initialization of other approaches. Indeed, in [31, 10] the registration between the pre-operative kidney model extracted from CT and the surface retrieved intra-operatively is achieved with a point-based approach, thanks to the presence of external markers visible in both the scenarios; then the registration is adjusted with surface-based method (Sec. 2.2.3). In [30, 38] the kidney model obtained from intra-operative CT is registered to the intra-operative surface by means of navigation aid inserted in the organ, so with a point-based registration, to initialize a surface-based method. However, in [34] the point-based registration is used to align the pre-operative kidney model to the intra-operative images: the anatomical landmarks are identified manually or with semiautomatic methods; the alignment has to be adjusted manually by the surgeon.

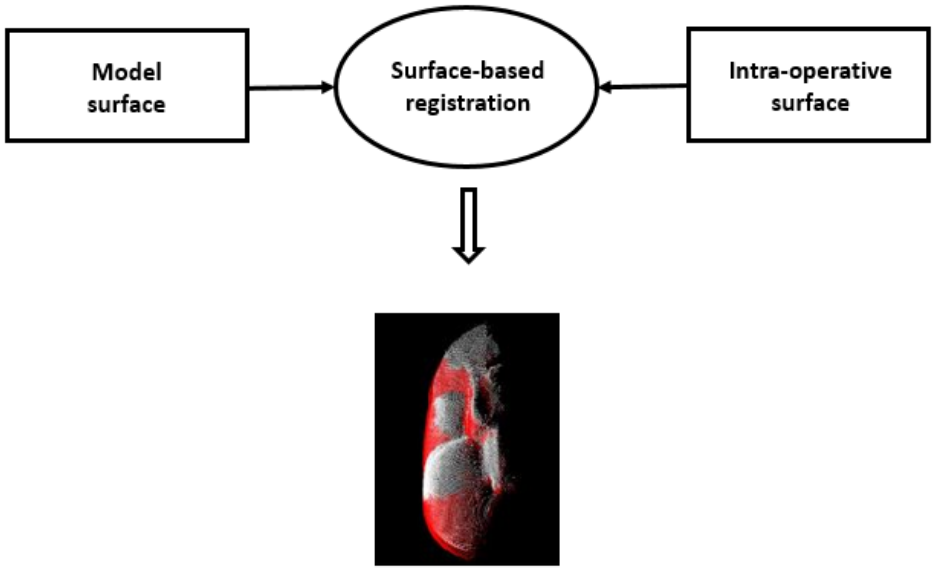

Figura 2.4: *The surface-based approach: the registration is performed between the pre-operative or intra-operative model surface (gray surface) and intra-operative surface (red surface). The resulting view is from [31].*

2.2.3 Surface-based approach

In the surface-based approach, the point cloud representing the model surface is rigidly or non-rigidly registered to the point cloud representing the surface extracted from the endoscopic images (Fig. 2.4). The registration workflow can be divided, as stated in [48], in:

- Pre-operative organ surface extraction: performed manually or with semi-automatic methods from high resolution anatomical images, such as MRI and CT. The point cloud representing the surface is retrieved.
- Laparoscopic scene surface reconstruction. The best accuracy in the laparoscopic view reconstruction is assured in case of stereo-vision. The optical reconstruction techniques are detailed described in [49]. The main limitation is the limited organ exposure in laparoscopy. The point cloud representing the surface is retrieved.
- Registration:
  - Initial rigid alignment: often performed with point-based strategies (Sec. 2.2.2) or manually (Sec. 2.2.1)
  - Automatic rigid or non-rigid refinement: the registration aims to reduce the distance between the two surfaces. The registration can be both rigid or deformable.

The described approach is used in [31, 10, 32, 33] to rigidly register the pre-operative model surface to the intra-operative surface after a point-based alignment (Sec. 2.2.2), in [30, 38] to rigidly register the intra-operative model surface to the intra-operative surface after a point-based alignment. In [40], the surface-based approach is used to non-rigidly register the pre-operative kidney model to the intra-operative surface (retrieved from the endoscopic images).

2.2.4 Volume-based approach

The volume-based approach (Fig. 2.5) is adopted when there is an intra-operative imaging system available to retrieve the intra-operative volume. The registration can

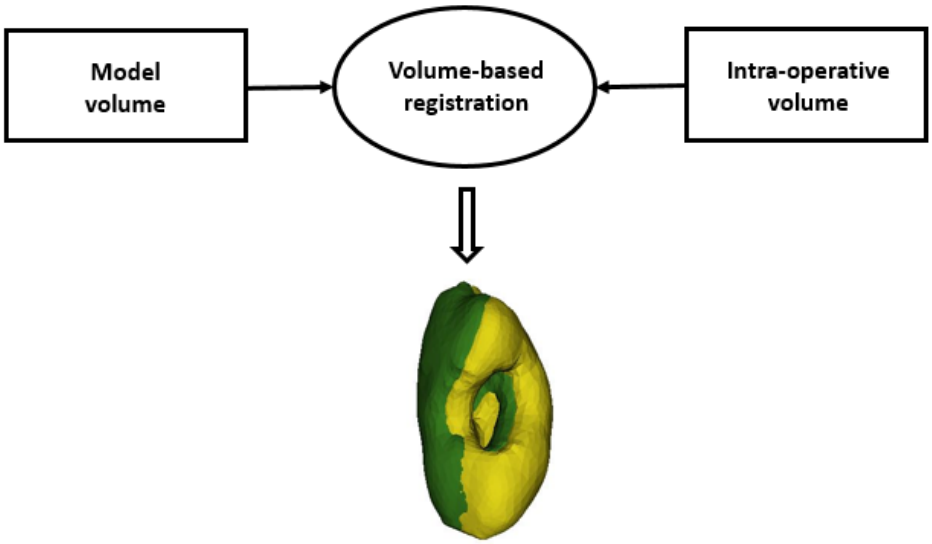

Figura 2.5: *The volume-based approach: the registration is performed between the pre-operative or intra-operative model volume (yellow) and intra-operative volume (green).*

be rigidly or non-rigidly performed.

There are two possible approaches:

- Registration of the pre-operative 3D volume to an intra-operative 3D volume with low resolution (usually the intra-operative volume is retrieved from low resolution imaging systems such as cone-beam CT and US). So the aim is to merge the exactly deformation of the organ (intra-operative volume) with the accurate anatomy (pre-operative volume).

- Registration of the intra-operative 3D volume to the surface reconstructed from endoscopic images: this approach avoids the extraction of the pre-operative model and allows the superimposition of the currently anatomy to the intra-operative scene.

An example of volume-based registration applied to kidney in reported in [39], where the kidney intra-operative model retrieved from low resolution CT is registered to the pre-operative model retrieved from high-resolution CT, after a point-based initialization (Sec. 2.2.2). The pre-operative model is deformed with a biomechanical model to mimic the intra-operative situation. The volumes are registered with a mean shift of 3 mm.

2.3 Limits in the registration literature for AR in nephrectomy

Regarding the approaches exposed in Sec. 2.2, some limitations can be highlighted.

The manual approach is strongly affected by the quality of its user interface and by the operator's degree of expertise.

In point-based approach, the limitations are related to the constraint on visibility of the same markers and to the tracking system inaccuracy. If the markers are manually identified, the degree of expertise affects the quality of the procedure.

In the surface-based approach, when implemented with deformable registration algorithm, the registration is reliable only for the visible surfaces, because no assumption is made on the underlying structure: this is an issue for big organs. The use of biomechanical model can alleviate this issues, but the parameters required by the used model have to be determined. Also the intra-operative surface reconstruction still is challenging. Instead, surface-based approach using rigid algorithms relies on the hypothesis of structure rigidity that is not true in the abdomen.

The limitations for the volume-based approach are the requirements of a hybrid OR (not always available and very expensive), the radiations delivered to the patient in case of cone-beam CT and the amount of data to be precessed and rendered (this limits the possibility to maintain the tracking during the procedure) Another limit is the degree of accuracy, that is influenced by all the systems involved (imaging systems, registration, tracking) [49].

Finally, nowadays the biggest limit is the absence of a system able to offer an accurate augmentation for nephrectomy. The most interesting system is [40], but it allows only the superimposition of the 2D tumor visible boundaries to the intra-operative endoscopic images, not considering the entire kidney surface (Sec. 1.3).

Chapter 3

MATERIALS AND METHODS

3.1 Methods

This Chapter will explain the proposed methodology adopted for the general workflow reported in Fig. 3.1. The pre-operative anatomical model was extracted from high resolution pre-operative images, as described in Sec. 3.1.1. The intra-operative point cloud was reconstructed from the endoscopic images and the strategy is described in Sec 3.1.2. To register the model and the point cloud, the registration was split in two parts (Sec. 3.1.3): (i) an initial alignment, mandatory for the next step, and (ii) an adjustment performed with the deformable registration algorithm to handle the problem of intra-operative scene deformation. For experimental purposes, kidney phantom were built as described in Sec. 3.1.4 to reconstruct an intra-operative point

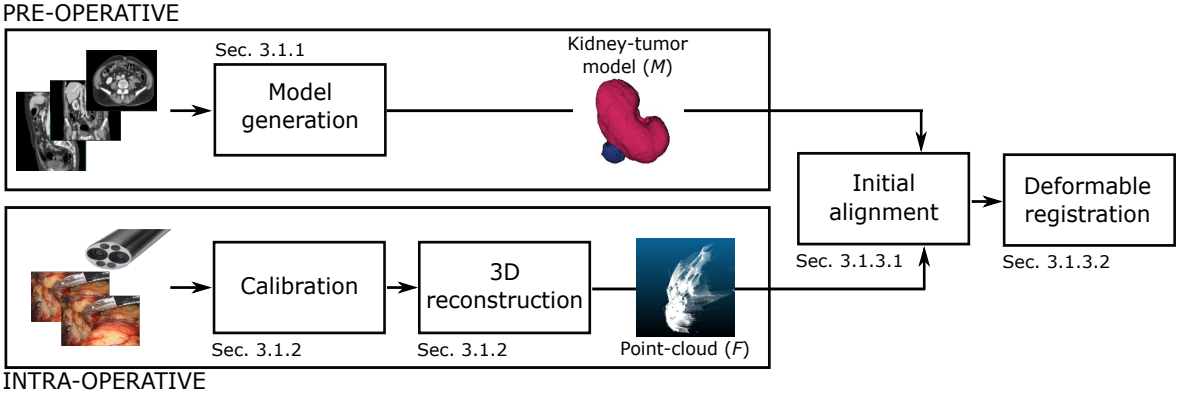

Figura 3.1: *The proposed registration workflow for augmented reality in nephrectomy.*

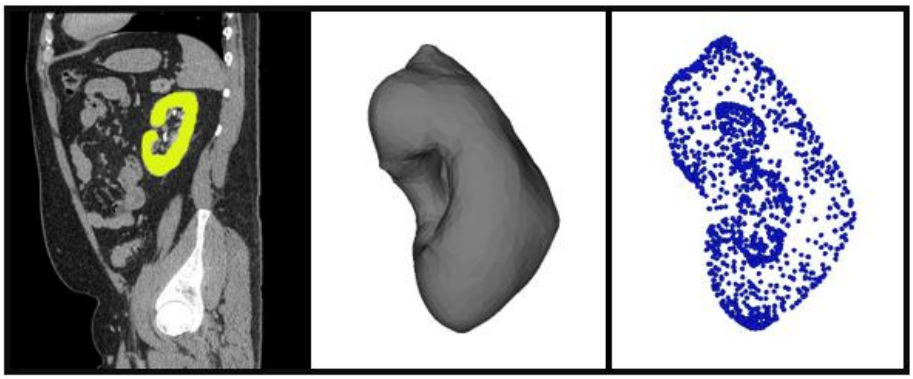

Figura 3.2: *The steps of the model generation: (left) segmentation of the computed tomography with active contours model; (center) kidney model obtained with fast marching method; (right) retrieved model vertexes (M).*

cloud.

3.1.1 Model generation

The pre-operative kidney anatomical model was extracted from pre-operative high resolution images. In this work, pre-operative abdominal CT were used. CT slices (Fig. 3.2 *left*) were segmented with a semiautomatic segmentation method exploiting deformable active contours model [50, 51]. It required a manual initialization: relevant structures were roughly identified by an operator. The deformable active contours model is a spline (i.e. an interpolation polynomial) dynamically altering its shape, being pulled towards object contours, while minimizing a merit function based on the energy of the spline itself.

From the obtained kidney segmentation mask, the kidney model (Fig. 3.2 *center*) was obtained with the Fast Marching Method (FMM) [52].

As a prerequisite for performing intra-operative registration (Sec. 3.1.3.2), the surface model vertexes (M) were retrieved from the obtained model (Fig. 3.2 *right*).

3.1.2 Calibration and 3D reconstruction

In order to perform the superimposition of the pre-operative model to the intra-operative point cloud, the kidney intra-operative surface visible in the endoscope had

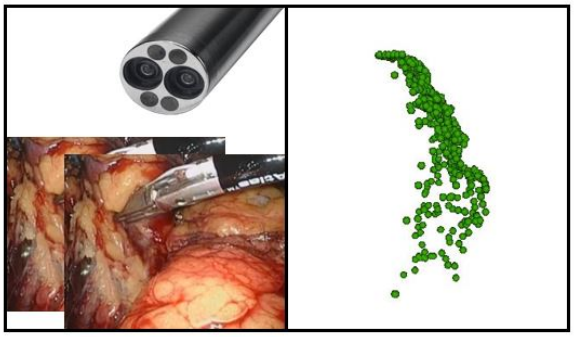

Figura 3.3: *The steps of the 3D reconstruction: (left) stereoimages acquired with the da Vinci Research Kit endoscope; (right) intra-operative point cloud retrieved with the dense soft-tissue 3D reconstruction.*

to be retrieved.

The kidney surface was acquired with dVRK endoscope (Fig. 3.3 *right*) and its point cloud (F) was retrieved from the endoscopic stereoimages (Fig. 3.3 *left*).

The camera calibration was performed according to the Zhang calibration method [53]. Zhang calibration method is a flexible method to model the radial lens distortion. A planar pattern was shown to the camera in at least two different orientation. From the acquired intra-operative stereoimages, dense soft-tissue 3D reconstruction was performed to retrieve F as in [54].

3.1.3 Registration

In this Section, the registration will be described. The used approach split the registration in two steps, the initial alignment and the deformable registration adjustment.

3.1.3.1 Initial alignment

The initial alignment aim was to put the intra-operative point cloud and the pre-operative one as closer as possible. This step was necessary given that a lot of registration algorithm, both rigid and deformable, require a good initialization to obtain an accurate registration.

There were two approaches for the initial alignment:

- **Manual initial alignment**: with a graphical user-interface, the pre-operative point cloud was aligned to the intra-operative one, moving manually the point

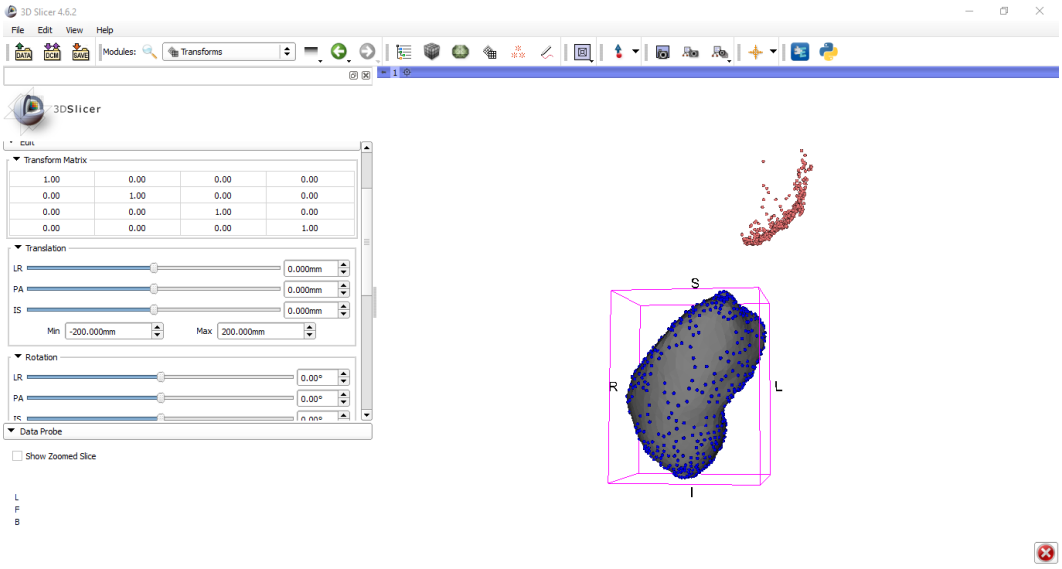

Figura 3.4: *The manual alignment was performed with the Slicer interface. The rotations angles and the values of translations were manually set.*

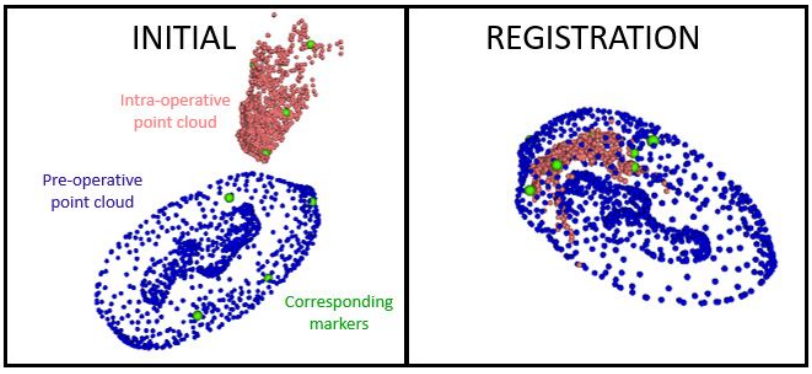

Figura 3.5: *Point-based registration of the kidney model to the intra-operative point cloud. (Left) From the kidney model vertexes ($\vec{p} \in P$, blue dots) and the intra-operative point cloud ($\vec{i} \in I$, pink dots), corresponding markers (green dots) were identified. (Right) The point-based registration was computed and the transformation was applied.*

cloud and adjusting the rotation angles and the translation parameters. An example implemented in Slicer[1], an open source software for medical image visualization and processing, is shown in Fig. 3.4.

- **Pair-point matching**: the adopted approach is the point-based one, thus two sets of corresponding markers, one from the intra-operative point cloud and one from the pre-operative one, with at least three corresponding points were necessary (in 3D). The rigid transformation necessary to superimpose the pre-operative markers ($p \in P$) to the intra-operative ones ($i \in I$) was retrieved. The transformation was found minimizing a cost function based on the distance (d) between the corresponding markers:

$$d(P, I) = \sum_{\vec{i} \in I} \min_{\vec{p} \in P} \|\vec{i} - \vec{p}\| \tag{3.1}$$

An example is shown in Fig. 3.5.

3.1.3.2 Deformable registration

Given the pre-operative model point cloud and the intra-operative point cloud, a surface-based approach was exploited. In particular, non-rigid FFD based on B-spline was used. FFD advantages, compared with other deformable registration algorithms described in Sec. 2.1, are the possibility to describe the deformation with a smooth function [46], the computational efficiency (due to the least number of contributing functions), the small b-splines overlap (that reduces the interdependency between variables), the flexibility (given no assumption on the underlying anatomy), the avoidance of one to one correspondence between point clouds(a control point is affected only by neighboring points) [55, 56, 57].

The main idea of FFD is to represent the kidney deformation of a moving point cloud (M) with respect to a reference or fixed point cloud (F) as the deformation of an underlying mesh (Φ) of control points ($\phi_{i,j,k}$) with n_x, n_y, and n_z control points along x, y and z axis, respectively (Fig. 3.6 *left* in 2D). Along each axis, the spacing is uniform: $\delta_x = \frac{dim_x}{n_x}$, $\delta_y = \frac{dim_y}{n_y}$, $\delta_z = \frac{dim_z}{n_Z}$, where dim_x, dim_x, dim_x are respectively

[1]https://www.slicer.org/

the point cloud dimension along x, y and z. The displacement in the control points is computed minimizing a cost function based on the Euclidean Distance ($d(M, F)$) between M and F (Eq. 2.2).

The transformation of a generic point $\vec{m} \in M$ with coordinates (x, y, z) was computed using a B-spline interpolation kernel:

$$T(x, y, z) = \sum_{l=0}^{3} \sum_{m=0}^{3} \sum_{n=0}^{3} B_l(u) B_m(v) B_n(w) \phi_{i+l, j+m, k+n} \tag{3.2}$$

where $i = |x/n_x| - 1$, $j = |y/n_y| - 1$, $k = |z/n_z| - 1$, $u = x/n_x - |x/n_x|$, $v = y/n_y - |y/n_y|$, $w = z/n_z - |z/n_z|$, and where $B_l(u)$, $B_m(v)$, $B_n(w)$ are the spline basis functions:

$$B_0(u) = \frac{(1-u)^3}{6}, \tag{3.3}$$

$$B_1(u) = \frac{3u^3 - 6u^2 + 4}{6}, \tag{3.4}$$

$$B_2(u) = \frac{-3u^3 + 3u^2 + 3u + 1}{6}, \tag{3.5}$$

$$B_3(u) = \frac{u^3}{6}. \tag{3.6}$$

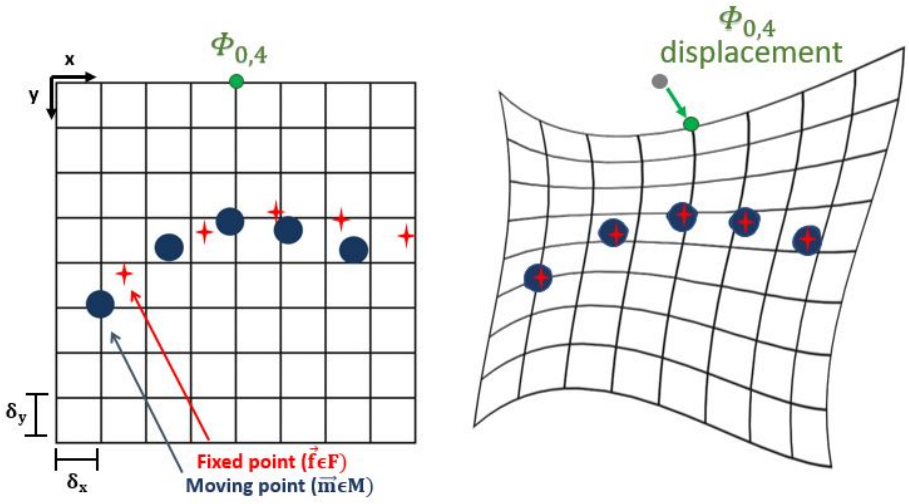

Figura 3.6: *The deformation of the control points ($\phi_{i,j}$) mesh Φ in Free Form Deformation model in 2D. (Left) Φ is built over the moving point cloud (blue dots). A cost function based on the distance between the moving point cloud and the fixed one (red stars) is minimized and the $\phi_{i,j}$ displacement is computed (the $\phi_{0,4}$ displacement in shown in green). (Right) the transformation retrieved is applied to all the moving points.*

The spline basis functions $B_l(u)$, $B_m(v)$, $B_n(w)$ are known for a given $\vec{m}$ and weight the contribution of each $\phi_{i,j,k}$ to $T(\vec{m})$ considering the distance between the point $\vec{m}$ and $\phi_{i,j,k}$. The optimization Levenberg-Marquardt algorithm (also known as Damped Least Squared method) [58, 59] was used to compute the optimal $\phi_{i,j,k}$ displacements. Once the optimal parameters are computed, the transformation can be applied to the moving points (Fig. 3.6 *right*).

The disadvantages of FFD are the requirement of a good initial alignment and the impossibility to deal with big rotation and with shearing.

3.1.4 Phantom development

To test the developed system, the development of kidney phantoms to allow the retrieval of a intra-operative point cloud was necessary. Phantoms were created through a moulding process as in [60]. The free and open source 3D creation suite Blender[2], was used: the 3D virtual negative molds were modeled staring from the pre-operative model computed as explained in Sec. 3.1.1. The virtual molds were 3D printed in acrylonitrile butadiene styrene (ABS), using the Elite Dimension 3D printer (layer thickness: 0.25mm). A bi-component silicon elastomer (Pro Lastix 10 A+B from Prochima s.r.l.)

[2]https://www.blender.org/

Figura 3.7: *The silicon kidney phantom obtained according to the pre-operative model.*

3.1.1 and used to acquire the intra-operative point cloud.

was combined with silicon oil (a softening agent) to mimic the real tissue stiffness. The silicon was colored to mimic the real appearance in the endoscopic view.

3.1.5 Implementation

The model generation explained in Sec. 3.1.1 was implemented in Slicer.

The 3D reconstruction described in Sec. 3.1.2 was implemented in C++.

The initial alignment (Sec. 3.1.3.1) was performed manually with Slicer while the pair point matching was implemented in C++ using the Visualization Toolkit (VTK) library, an open-source, freely available software system for 3D computer graphics, image processing, and visualization[3].

The deformable registration algorithm (Sec. 3.1.3.2) and the rigid ICP registration algorithm, used for the comparison, were implemented in C++ using the Insight Segmentation and Registration Toolkit (ITK) library, an open-source, cross-platform system for image analysis[4].

3.2 Materials

The workflow explained in Sec. 3.1 was tested on different datasets. As pre-operative model point cloud, two models were used ($M1$ and $M2$). $M1$ was a patient kidney

[3]https://www.vtk.org/
[4]https://itk.org/

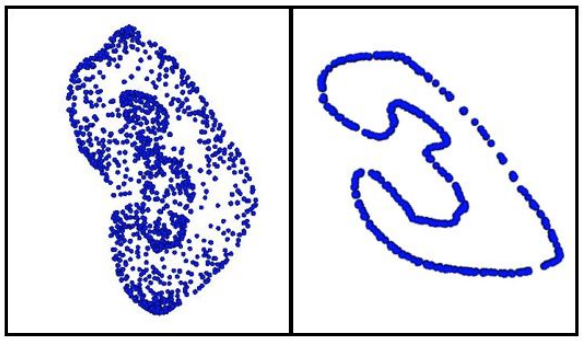

Figura 3.8: *(Left) 3D model point cloud; (right) model point cloud in 2D obtained retrieving the 2D boundaries of the 3D model projected on a plane.*

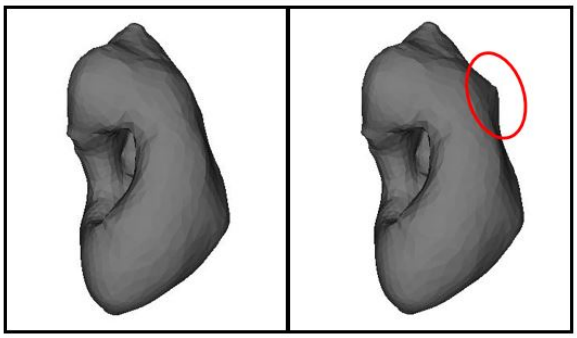

Figura 3.9: *(Left) kidney model; (right) kidney model deformed with the open source 3D creation suite Blender to test the registration in a controlled environment.*

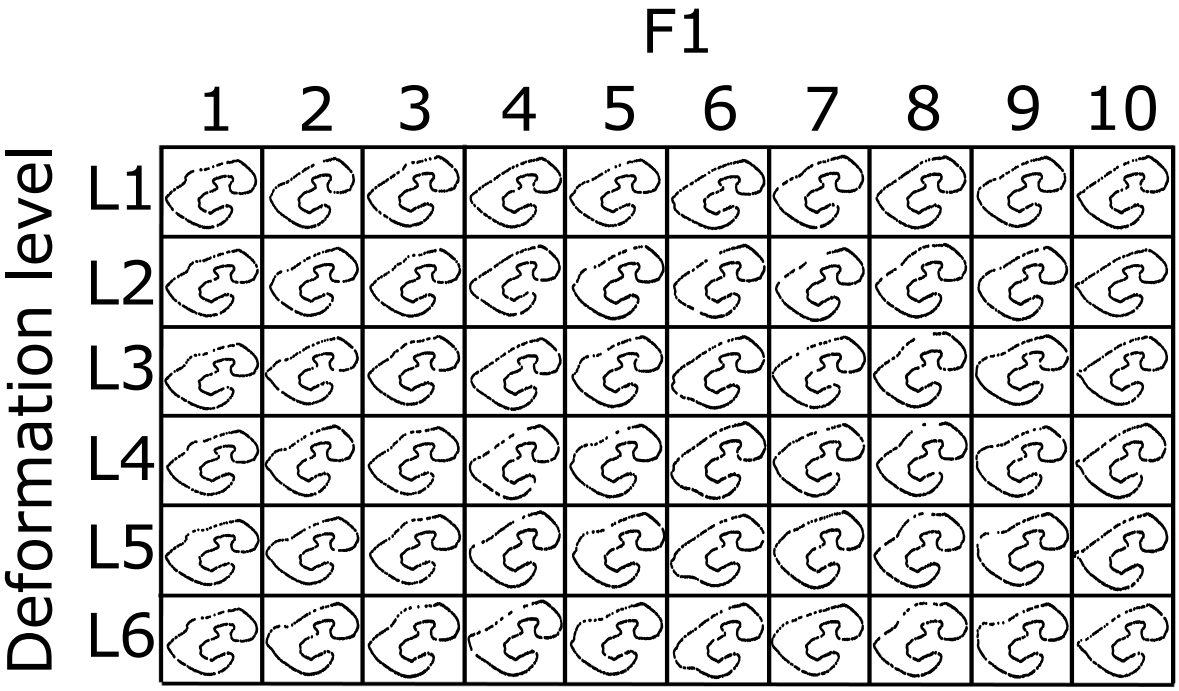

Figura 3.10: *The 2D intra-operative point clouds (F1) manually obtained from the 2D kidney model boundary. Starting from ten different positions on the model cloud, the deformation is progressively increased from L1 (the smallest) to L6 (the biggest).*

model obtained from anonymized Ircadb2 dataset[5]. The Ircadb2 dataset contained the abdominal CT volume of a male patient, with 512x512x167 slices and a voxel size of 0.916x0.916x1.8 mm. It also contained the models of all visible organs, obtained with manual segmentation and FMM. $M2$ was retrieved from anonymized CT given by Istituto Europeo di Onconologia (IEO). The CT contained the abdominal volume of a male patient, with 512x512x716 slices and a voxel size of 0.703x0.703x0.625 mm. The CT slices were segmented and the model was retrieved according to Sec. 3.1.1. The pre-operative model was used both entire (3D) and in form of 2D boundary, obtained by projecting the point cloud on a plane and retrieving the projection boundary (Fig. 3.8). As intra-operative point cloud, two point clouds were used ($F1$ and $F2$). $F1$ was obtained by manually deforming the $M1$ with the software Blender (Fig 3.9). The deformation was aimed to replicate tissue-surgical tool interactions and tissue manipulation. $F1$ was made to test the registration algorithm in a controlled environment, without noise but with completely controlled degree of deformation. The 2D $F1$ used are reported in Fig. 3.10: a dataset of 60 $F1$ was built deforming the $M1$ in different point and progressively increasing the deformation level (from the smallest deformation L1 to the biggest L6; L3 was considered the medium deformation level). A dataset in 3D was build following the same criteria, so, in ten different locations, the 3D point cloud was deformed with six deformation levels (from L1 to L6). To test the workflow in a more realistic situation, $F2$ was retrieved acquiring the stereoimages on the kidney silicon phantom and reconstructing the point cloud according to Sec. 3.1.2.

3.3 Evaluation protocol

The developed system was tested to investigate its ability to deal with kidney deformation. To test the registration performance, the Root Mean Squared Error (RMSE) was compared before ($RMSE_{initial}$) and after ($RMSE_{final}$) the registration. The RMSE reduction ($-\Delta_{RMSE}$) is defined as:

$$-\Delta_{RMSE} = \frac{RMSE_{initial} - RMSE_{final}}{RMSE_{initial}} \tag{3.7}$$

where $RMSE = \sqrt{d(M,F)}$, with $d(M,F)$ defined in Eq. 2.2.

[5]https://www.ircad.fr/research/3d-ircadb-02/

The performances of deformable registration in the experiments (E), reported in Tab. 3.1, were evaluated.

3.3.1 E1: investigation of n_x and n_y

The differences in terms of $-\Delta_{RMSE}$ using different values of n_x and n_y was done arbitrarily fixing them and computing the results. The evaluation was made in 2D for sake of simplicity. Arbitrarily fixing n_x and n_y led to $\delta_x \neq \delta_y$, thus the comparison with the use of the same δ along the two directions x and y was done, too. The test was performed on $M1$ and ten $F1$ (medium deformation L3). The investigation on the use of not arbitrarily fixed n_x and n_y was done also to have a Φ formulation as general as possible.

3.3.2 E2: trade-off between number of iteration and $-\Delta_{RMSE}$

The relation in FFD between the number of iterations ($iter_{max}$) and the $-\Delta_{RMSE}$ was investigated in order to determine the best trade-off between the computational time required by the iterations and the registration accuracy. The experiment was performed knowing the best δ from *E1.* The test was performed in 2D, for sake of simplicity, using ten $F1$ (L3 deformation level). The time required, using a PC with AMD Ryzen 7 and 32 GB of RAM, was reported, too.

3.3.3 E3: Comparison between FFD and ICP in 2D

A comparison was made between FFD and ICP accuracy ($-\Delta_{RMSE,ICP}$ and $-\Delta_{RMSE,FFD}$), in 2D, registering the 2D $M1$ to the $F1$ dataset reported in Fig. 3.10. The aim of the analysis is (i) to compare, for each deformation level, the $-\Delta_{RMSE,ICP}$ and $-\Delta_{RMSE,FFD}$ with the non-parametric Wilcoxon test ($\alpha = 0.05$) to investigate the presence of significant difference using the rigid or the deformable algorithm for the presented dataset; (ii) to investigate the presence of significant differences (Wilcoxon test, $\alpha = 0.05$) in $-\Delta_{RMSE,FFD}$ according to the deformation level ($-\Delta_{RMSE,FFD}$ for L1 compared to $-\Delta_{RMSE,FFD}$ for L2, compared to $-\Delta_{RMSE,FFD}$ for L3 and so on); the same was done to compare $-\Delta_{RMSE,ICP}$ according to the deformation level.

3.3.4 E4: Comparison between FFD and ICP in 3D

This experiment had the same aims of *E3*, however it was performed registering the 3D $M1$ to the 3D $F1$ dataset.

3.3.5 E5: Registration of $M1$ to $F2$ with manual initial alignment

The experiments was made to test the proposed workflow to register $M1$ to $F2$, i.e. the point cloud acquired on the kidney phantom. The workflow adopted is: (i) manual initial alignment, (ii) deformable registration refinement. The $RMSE_{before}$, i.e. RSME before the manual alignment, the $RMSE_{alignment}$, i.e. RMSE after the alignment, and the $RMSE_{registration}$, i.e. RMSE after the deformable registration, were considered to measure the quality of the overall registration workflow. A trail was performed using part of the kidney model.

3.3.6 E6: Registration of $M2$ to $F2$ with manual initial alignment

This experiment followed the same steps of *E5* in Sec. 3.3.5 to register the entire $M2$ and a part of $M2$ to $F2$.

3.3.7 E7: Registration of $M1$ to $F2$ with point-based initial alignment

The workflow adopted was: (i) point-based initial alignment with four corresponding points manually identified in $M1$ and in $F2$, (ii) deformable registration refinement. The quality of the overall workflow was measured as reported in Sec. 3.3.5. A trail was performed using part of the kidney model.

3.3.8 E8: Registration of $M2$ to $F2$ with point-based initial alignment

This experiment followed the same steps of *E7* in Sec. 3.3.7 to register the entire $M2$ and a part of $M2$ to $F2$.

Experiment	Investigation	Data
E1	Uniform δ	M1 and 10 F1 (medium deformation) in 2D
E2	$iter_{max}$ and $-\Delta_{RMSE}$ trade-off	M1 and 10 F1 (medium deformation) in 2D
E3	FFD vs ICP	M1 and 10 F1 with 6 deformation in 2D
E4	FFD vs ICP	M1 and 10 F1 with 6 deformation in 3D
E5	Registration workflow (manual initial alignment)	M1 and F2
E6	Registration workflow (manual initial alignment)	M2 and F2
E7	Registration workflow (point-based initial alignment)	M1 and F2
E8	Registration workflow (point-based initial alignment)	M2 and F2

Tabella 3.1: *$M1$ was the model vertexes point cloud obtained from the Ircadb Computed Tomography (CT) with manual segmentation and Fast Marching Method (FFM) reconstruction. $M2$ was the model vertexes point cloud obtained segmenting (deformable model active contours) and reconstructing (FFM) an abdominal CT from the Istituto Europeo di Oncologia. $F1$ was the intra-operative point cloud obtained manually deforming $M1$ with Blender, an open source software. $F2$ was the intra-operative point cloud retrieved from the da Vinci Reseach Kit's endoscopic acquisitions on kidney silicon phantom (dense soft-tissue 3D reconstruction). FFD was the Free Form Deformation registration algorithm, based on a mesh grid whose control points are separated by spacing δ. ICP was the Iterative Closest Point rigid registration algorithm. $iter_{max}$ is the maximum number of iteration of the registration algorithm. $-\Delta_{RMSE}$ is the Root Mean Square Error (RMSE) reduction.*

Chapter 4

RESULTS

The results of the experiments described in 3.3 will be shown in this section.

The results of *E1* are reported in Tab. 4.1. The best $-\Delta_{RMSE}$ were obtained using a uniform δ or a low number of $\phi_{i,j}$ (6,6 and 5,5). Thus, to maintain the generality and to not fix a priori the n_x and n_y, a uniform δ was used in the other experiments.

In Fig. 4.1, the results of the experiment *E2* are reported: after few iterations, the $-\Delta_{RMSE}$ always reached a plateau. So, given all the tested cases reached an almost constant $-\Delta_{RMSE}$ after 1000, the $iter_{max}$ was fixed at 1000 for the other experiments. The Tab. 4.2 reports the relation between the $iter_{max}$ and the mean computational time required.

The boxplots represented in Fig. 4.2 show, for the 2D case, the comparison between $-\Delta_{RMSE,ICP}$ and $-\Delta_{RMSE,FFD}$ for the six deformation levels of *E3*. Significant differences between $-\Delta_{RMSE,ICP}$ and $-\Delta_{RMSE,FFD}$ was assured by the Wilcoxon tests (p-value $< \alpha$). The results of the comparison between the $-\Delta_{RMSE,ICP}$ and $-\Delta_{RMSE,FFD}$ according to the deformations levels are shown in Fig. 4.3. No significant difference was found, so the level of initial deformation had not effects on the registration accuracy. In Fig. 4.4 an example of the application of FFD in the 2D case is displayed: on the *left* there is the initial situation, on *right* the registration result.

The boxplots in Fig. 4.5 represent *E4* results for the 3D case. The comparison of $-\Delta_{RMSE,ICP}$ and $-\Delta_{RMSE,FFD}$ according to the deformations levels are shown in Fig. 4.6.

n_x, n_y	Mean $-\Delta_{RMSE}$
10,10	0.30
6,6	0.44
5,5	0.44
$\frac{dim_x}{5}, \frac{dim_y}{5}$	0.30
$\frac{dim_x}{8}, \frac{dim_y}{8}$	0.31
$\frac{dim_x}{10}, \frac{dim_y}{10}$	0.32
$\frac{dim_x}{15}, \frac{dim_y}{15}$	0.45
$\frac{dim_x}{20}, \frac{dim_y}{20}$	0.44

Tabella 4.1: *Expetiment E1 results.* n_x *and* n_y *were the number of control points along the x and y direction, respectively.* Δ_{RMSE} *was the Root Mean Square Error (RMSE) reduction.* dim_x *and* dim_y *were the reference point cloud dimensions along x and y.*

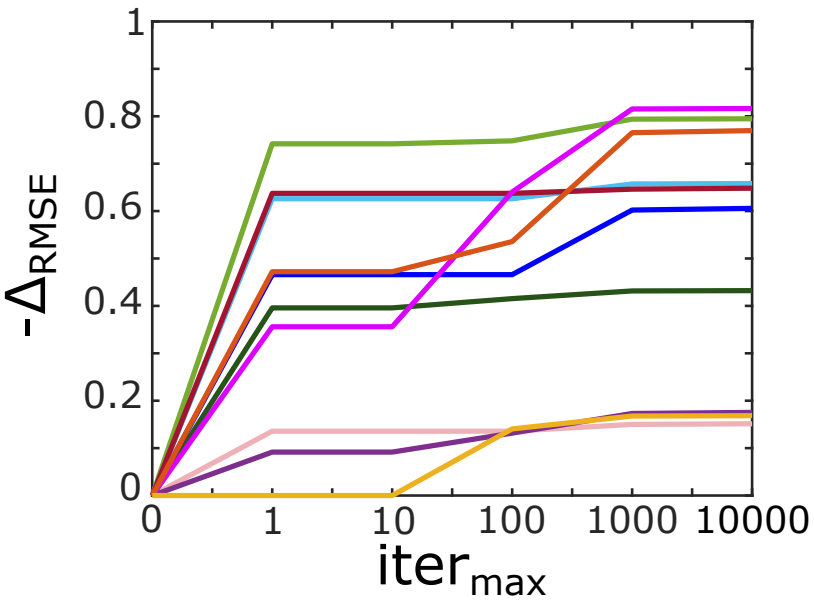

Figura 4.1: *Experiment E2 results.* $-\Delta_{RMSE}$ *was the Root Mean Square Error (RMSE) reduction and* $iter_{max}$ *was the maximum number of iteration. The results were obtained registering in 2D with Free Form Deformation algorithm the model boundary to ten manually deformed boundary with medium deformation level.*

$iter_{max}$	Mean computational time [s]
1	2.4
10	2.5
100	5
1000	30
10000	286

Tabella 4.2: *Relation between the maximum number of iteration ($iter_{max}$) and the computational time in Free Form Deformable registration algorithm for E2. The mean computational time was computed on the registration of the 2D model boundary to ten manually deformed kidney boundary with medium deformation level.*

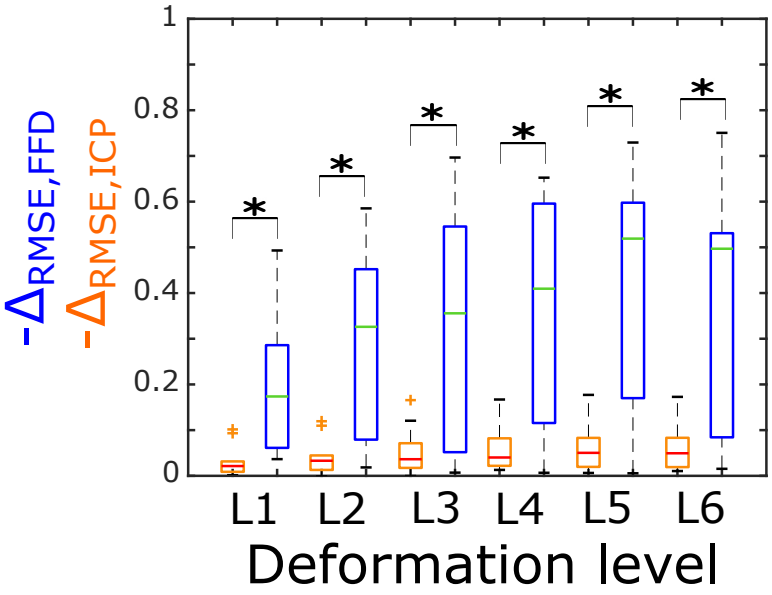

Figura 4.2: *Experiment E3 results. On the horizontal axis are reported the deformation levels (L) of the manually deformed boundary (the intra-operative point cloud to which the model boundary was registered). The $-\Delta_{RMSE,ICP}$ was the Root Mean Square Error (RMSE) reduction of Iterative Closest Point (ICP) algorithm (orange). The $-\Delta_{RMSE,FFD}$ was the RMSE reduction of Free Form Deformation (FFD) algorithm (blue). Statistical significant difference (given by Wilcoxon test with $p < \alpha$) are represented with a star.*

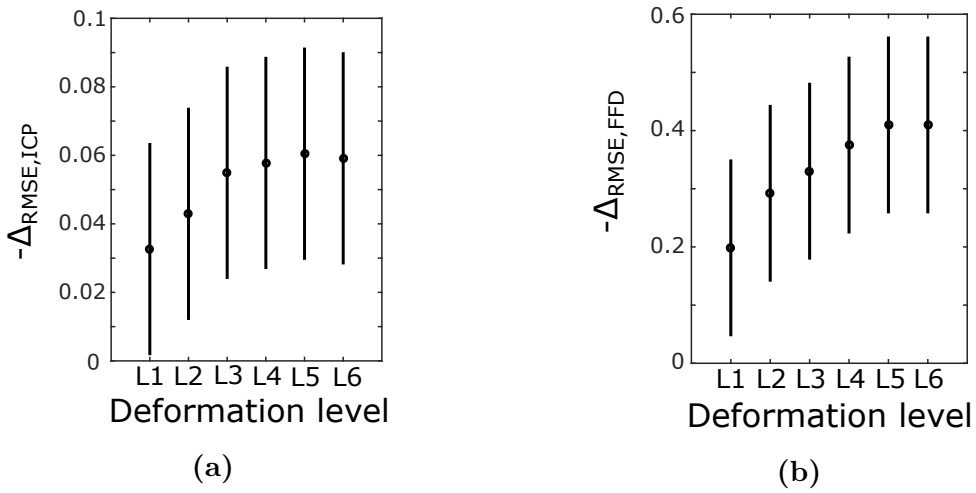

Figura 4.3: *Experiment E3 results.* $-\Delta_{RMSE,ICP}$ *(a) was the Root Mean Square Error (RMSE) reduction for Iterative Closest Point (ICP) registration algorithm and* $-\Delta_{RMSE,FFD}$ *(b) was the RMSE reduction for FFD algorithm. On the horizontal axis the deformation levels (L) of the manually deformed boundary to which the model boundary was registered are represented. The absence of significant difference is represented with black lines.*

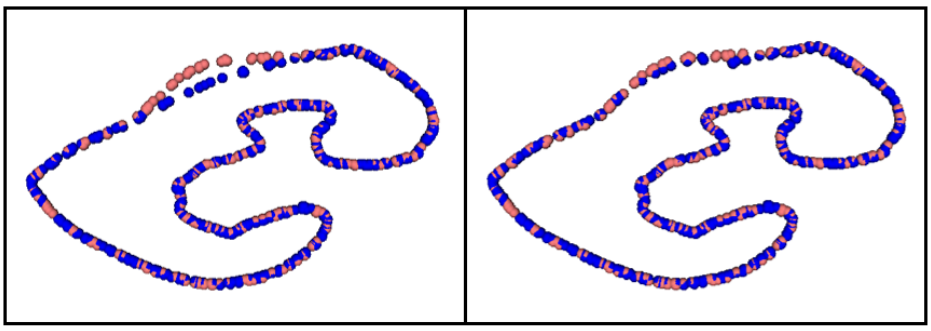

Figura 4.4: *An example of deformable registration results from experiment E3. (Left) Initial situation: the blue point cloud was the pre-operative model boundary and the pink point cloud was the manually deformed point cloud. (Right) After deformable registration.*

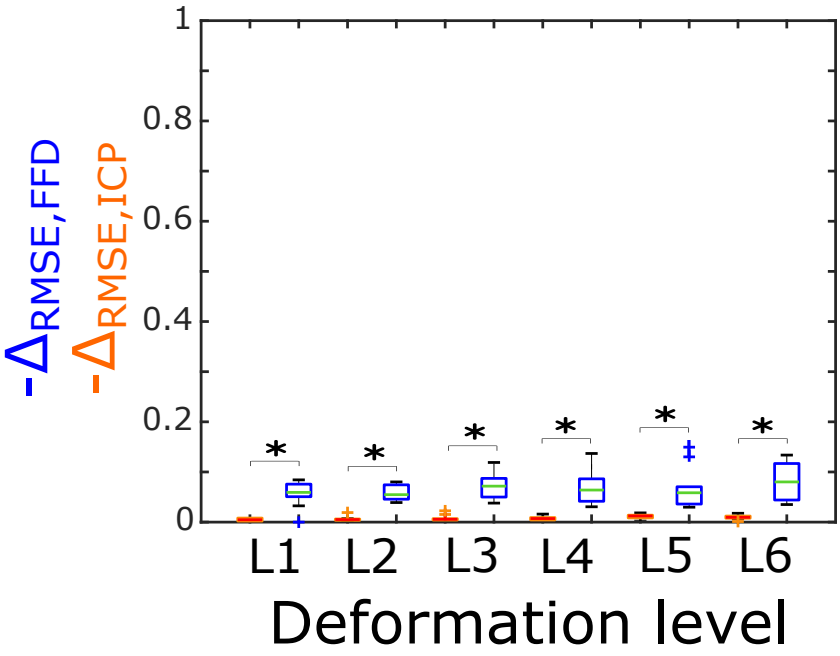

Figura 4.5: *Experiment E4 results. On the horizontal axis are reported the deformation levels (L) of the manually deformed boundary (the intra-operative point cloud to which the model boundary was registered). The $-\Delta_{RMSE,ICP}$ was the ROot Mean Square Error (RMSE) reduction of Iterative Closest Point (ICP) algorithm (orange). The $-\Delta_{RMSE,FFD}$ was the RSME reduction of Free Form Deformation (FFD) algorithm (blue). Statistical significant difference (given by Wilcoxon test with $p < \alpha$) are represented with a star.*

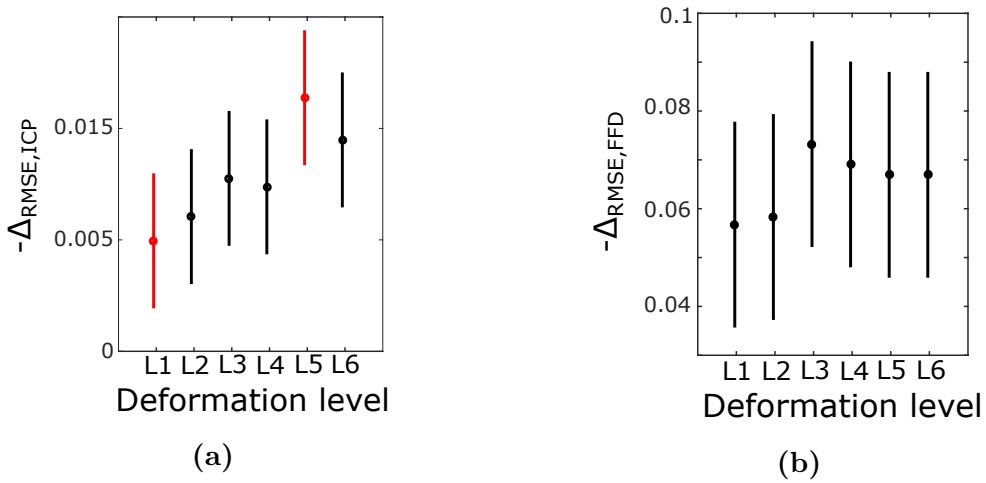

Figura 4.6: *Experiment E4 results.* $-\Delta_{RMSE,ICP}$ *(a) was the Root Mean Square Error (RMSE) reduction for Iterative Closest Point (ICP) registration algorithm and* $-\Delta_{RMSE,FFD}$ *(b) was the RMSE reduction for FFD algorithm. On the horizontal axis the deformation levels (L) of the manually deformed boundary to which the model boundary was registered are represented. The absence of significant difference is represented with black lines, while the presence of significant difference is represented with red lines.*

Experiment	$RMSE_{before}$ [mm]	$RMSE_{alignment}$ [mm]	$RMSE_{registration}$ [mm]
E5 on entire $M1$	59.2	34.8	30.6
E5 on part of $M1$	60.9	21.9	17.7
E6 on entire $M2$	299.5	32.2	27.8
E6 on part of $M2$	131.3	20.2	19.2
E7 on entire $M1$	59.2	19.1	18.6
E7 on part of $M1$	59.0	18.0	16.9
E8 on entire $M2$	299.5	43.1	40.4
E8 on part of $M2$	132.2	21.1	15.1

Tabella 4.3: *Epxeriments E5, E6, E7, E8 results.* $RMSE_{before}$ *was the Root Mean Square Error (RMSE) before the registration,* $RMSE_{alignment}$ *was the RMSE after the alignment, used to initialize the registration, and* $RMSE_{registration}$ *was the RMSE after the deformable registration. The experiments protocol are reported in Tab. 3.1.* $M1$ *was the model obtained from the Irbadb2 Computed Tomography (CT) with manual segmentation and Fast Marching Method (FMM) reconstruction,* $M2$ *was the model obtained from CT from Istituto Europeo di Oncologia with deformable model active contour segmentation and FMM reconstruction.*

Experiment	$-\Delta_{RMSE,initialalignment}$	$-\Delta_{RMSE,deformableregistration}$
E5 on entire $M1$	0.41	0.12
E5 on part of $M1$	0.64	0.19
E6 on entire $M2$	0.89	0.14
E6 on part of $M2$	0.85	0.05
E7 on entire $M1$	0.68	0.03
E7 on part of $M1$	0.69	0.06
E8 on entire $M2$	0.86	0.06
E8 on part of $M2$	0.84	0.28

Tabella 4.4: *Experiments E5, E6, E7, E8 results.* $-\Delta_{RMSE,initialalignment}$ *was the Root Mean Square Error (RMSE) reduction in the initial alignment, performed according to the experimental protocol, and* $-\Delta_{RMSE,deformableregistration}$ *was the RMSE reduction in the deformable registration. The experiments protocol are reported in Tab. 3.1.* $M1$ *was the model obtained from the Irbadb2 Computed Tomography (CT) with manual segmentation and Fast Marching Method (FMM) reconstruction,* $M2$ *was the model obtained from CT from Istituto Europeo di Oncologia with deformable model active contour segmentation and FMM reconstruction.*

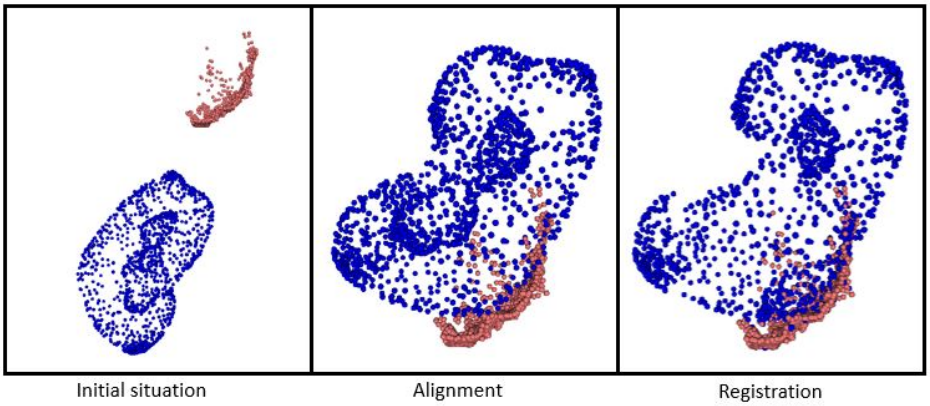

Figura 4.7: *Experiment E5 results obtained with the entire kidney model. (Left) Initial situation: the blue point cloud was the pre-operative model and the pink point cloud was the intra-operative surface acquired on kidney phantom. (Center) The alignment was performed manually. (Right) After deformable registration.*

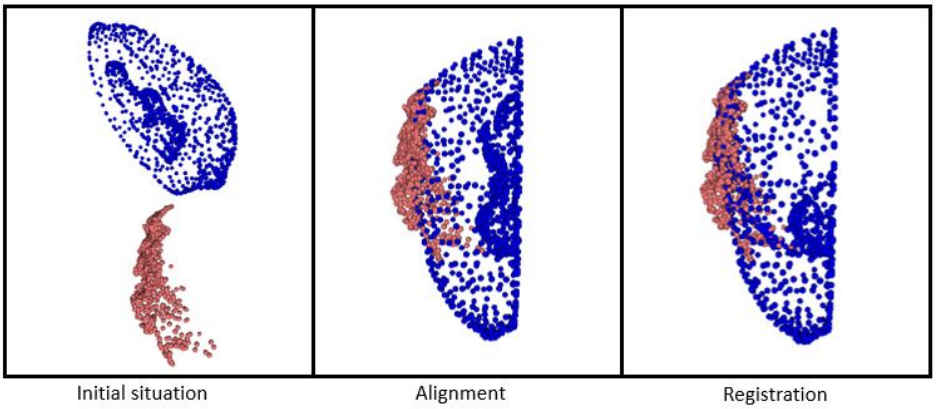

Figura 4.8: *Experiment E5 results obtained with part of the kidney model. (Left) Initial situation: the blue point cloud was the pre-operative model and the pink point cloud was the intra-operative surface acquired on kidney phantom. (Center) The alignment was performed manually. (Right) After deformable registration.*

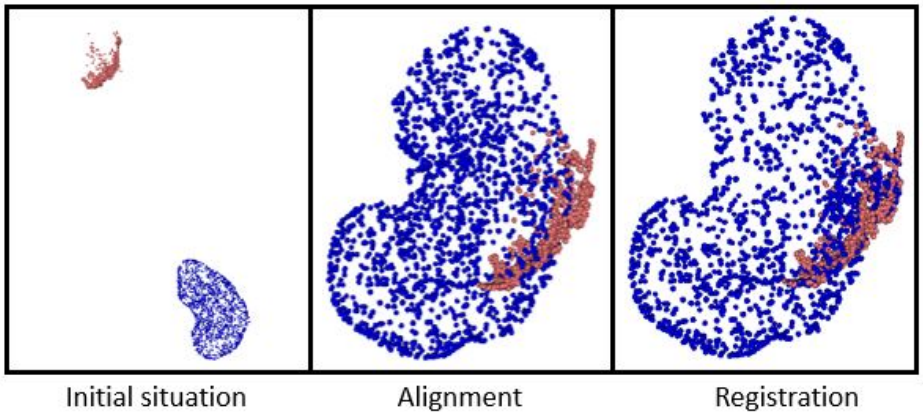

Figura 4.9: *Experiment E6 results obtained with the entire kidney model. (Left) Initial situation: the blue point cloud was the pre-operative model and the pink point cloud was the intra-operative surface acquired on kidney phantom. (Center) The alignment was performed manually. (Right) After deformable registration.*

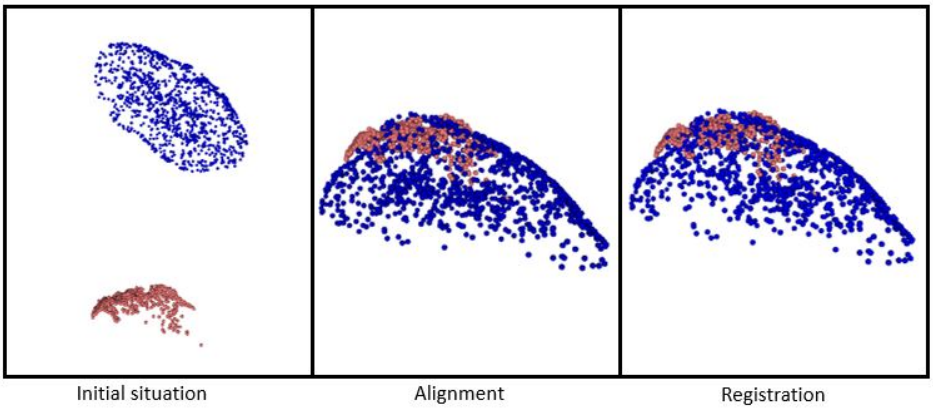

Figura 4.10: *Experiment E6 results obtained with part of the kidney model. (Left) Initial situation: the blue point cloud was the pre-operative model and the pink point cloud was the intra-operative surface acquired on kidney phantom. (Center) The alignment was performed manually. (Right) After deformable registration.*

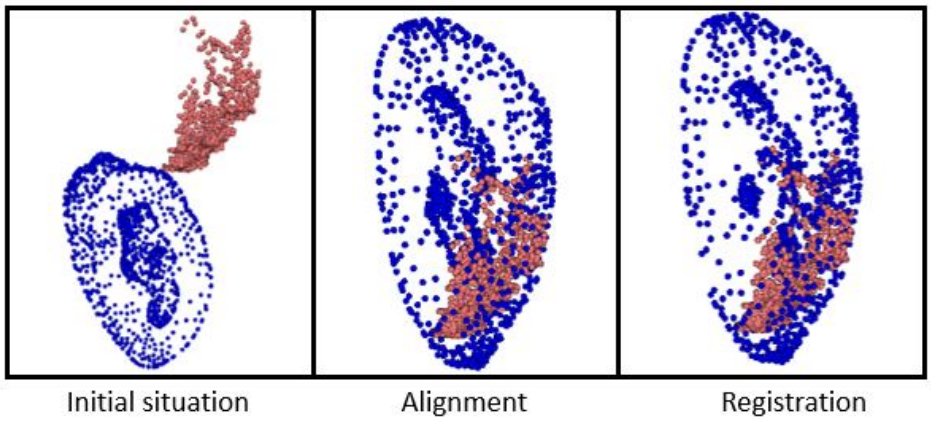

Figura 4.11: *Experiment E7 results obtained with the entire kidney model. (Left) Initial situation: the blue point cloud was the pre-operative model and the pink point cloud was the intra-operative surface acquired on kidney phantom. (Center) The alignment was performed with markers. (Right) After deformable registration.*

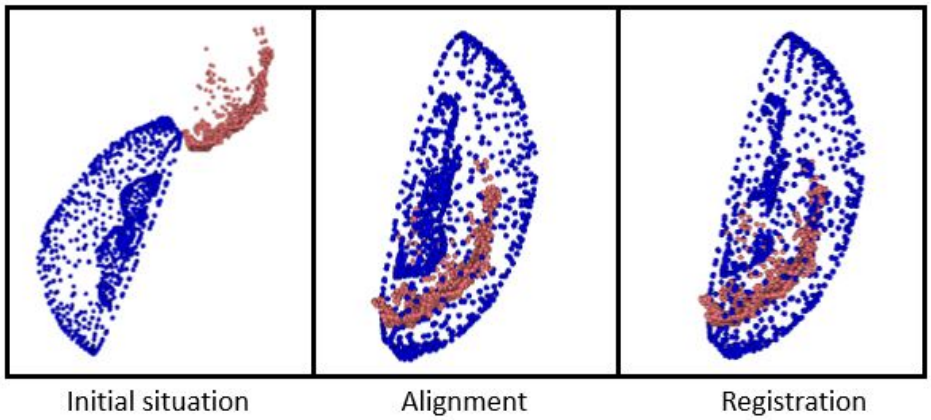

Figura 4.12: *Experiment E7 results obtained with part of the kidney model. (Left) Initial situation: the blue point cloud was the pre-operative model and the pink point cloud was the intra-operative surface acquired on kidney phantom. (Center) The alignment was performed with markers. (Right) After deformable registration.*

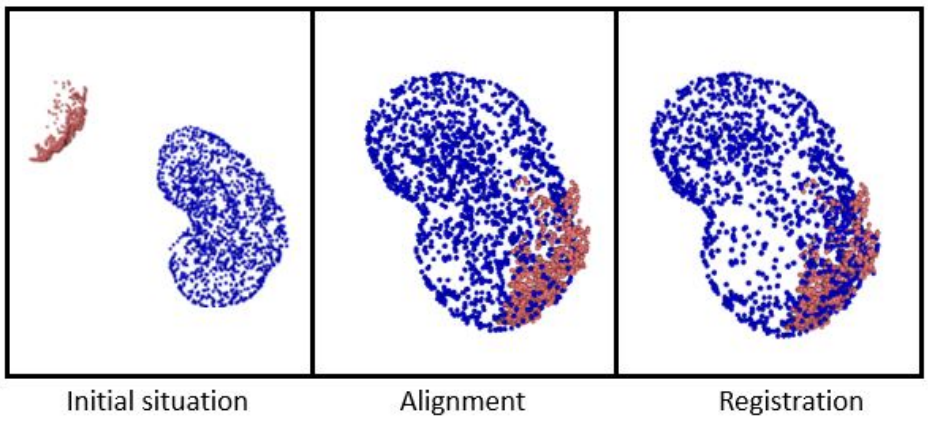

Figura 4.13: *Experiment E8 results obtained with the entire kidney model. (Left) Initial situation: the blue point cloud was the pre-operative model and the pink point cloud was the intra-operative surface acquired on kidney phantom. (Center) The alignment was performed with markers. (Right) After deformable registration.*

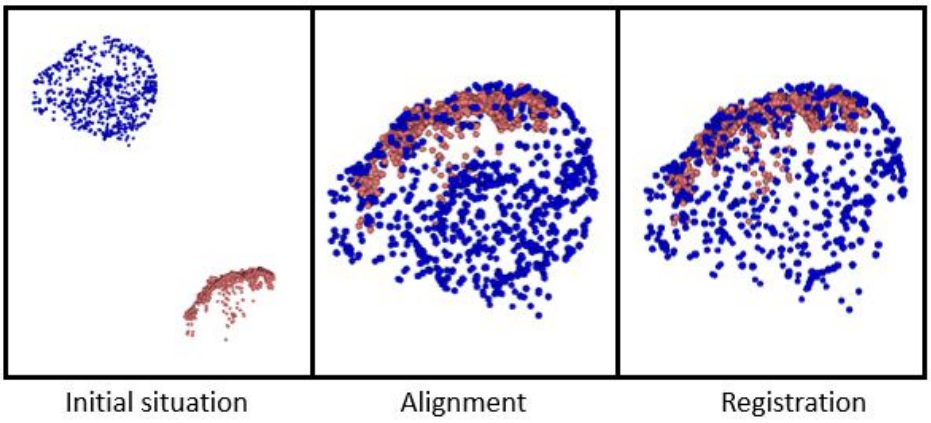

Figura 4.14: *Experiment E8 results obtained with part of the kidney model. (Left) Initial situation: the blue point cloud was the pre-operative model and the pink point cloud was the intra-operative surface acquired on kidney phantom. (Center) The alignment was performed with markers. (Right) After deformable registration.*

The results of the entire workflow *E5* experiment on the entire kidney model is displayed in Fig. 4.7, while the result obtained using only part of the kidney is shown in Fig. 4.8. On the *left* the initial situation is shown, in the *center* there is the result of the alignment and on the *right* the deformable registration result is shown. The Fig. 4.9 and 4.10 show the *E6* results, respectively, using the entire model and using only a portion of it. The *E7* results, for the entire model and for a part of it, are shown in Fig. 4.11 and 4.12. The Fig. 4.13 and 4.14 show the *E8* results, respectively, using the entire model and using only a portion of it.

For the experiments *E5*, *E6*, *E7*, *E8*, the RMSE of the initial situation ($RMSE_{before}$), the RMSE after the alignment ($RMSE_{alignment}$), that is performed manually or with point-based approach according to the considered experiment, and the RMSE after the deformable registration ($RMSE_{registration}$) are reported on Tab. 4.3. The values of $-\Delta_{RMSE,initialalignement}$ and of $-\Delta_{RMSE,deformableregistration}$ computed from the values of Tab. 4.3 are shown in Tab. 4.4.

Chapter 5

DISCUSSION

In this Chapter, the results presented in Sec. 4 will be discussed.

First of all, the $\phi_{i,j}$ distribution was investigated in 2D (*E1*): the best $-\Delta_{RMSE}$ were obtained using a coarse Φ and so a low n_x and n_y ($-\Delta_{RMSE}$ of 0.44 both for $n_x = 5$,$n_y = 5$ and for $n_x = 6$,$n_y = 6$). However, using fixed n_x and n_y did not assure the possibility to use the same workflow for a point cloud with different size, so the $-\Delta_{RMSE}$ resulting from the use of n_x and n_y depending on dim_x and dim_y were more interesting. Moreover, it was found that using $n_x = \frac{dim_x}{15}$ and $n_y = \frac{dim_y}{15}$ the $-\Delta_{RMSE}$ was a little bit better (0.45). The relation of $-\Delta_{RMSE}$ with the $\phi_{i,j}$ distribution is stated in the formulation of the transformation in FFD (Eq. 3.2): $T(\vec{m})$ is influenced by a fixed number of surrounding control points and, if they are distant (i.e. Φ is coarse), the area identified by them is wide, therefore $T(\vec{m})$ is influenced by the deformation occurred in that wide area. Otherwise, $T(\vec{m})$ is influenced by the deformation in a small area, not taking into account the entire deformation. Thus, for sake of generality and to take into account the actual dimension of the point cloud, $n_x = \frac{dim_x}{15}$ and $n_y = \frac{dim_y}{15}$ were used in all the experiments (adding $n_z = \frac{dim_z}{15}$ when working on 3D).

The computational time was investigated comparing the $-\Delta_{RMSE}$ obtained varying $iter_{max}$ for ten $F1$. As it is possible to see in the *E2* results (Fig. 4.1), for all the tested dataset, the $-\Delta_{RMSE}$ increased a lot in the first few iterations, while after approximatively 1000 iterations it reached a plateau. Thus, it is possible to limit

the number of iterations without affecting the registration accuracy. The mean time required to perform 1000 iterations was 30 seconds. These results shows that FFD algorithm is a possible option for the implementation of an almost real time system able to augment the scene.

The proposed deformable algorithm was used to register the 2D model boundary to the manually deformed $F1$ dataset (*E3*) and its results ($-\Delta_{RMSE,FFD}$) were compared with the one obtained with ICP ($-\Delta_{RMSE,ICP}$). The algorithm parameters were fixed according to the previous described results to achieve a good $-\Delta_{RMSE}$ with the minimum computational time. The registration was performed with the manual created $F1$ to test in a controlled environment and with controlled deformation levels. The comparison between $-\Delta_{RMSE,FFD}$ and $-\Delta_{RMSE,ICP}$, separated according to the deformation levels, showed that there was a statistically significant difference (Wilcoxon test with $\alpha = 0.05$ rejected the hypothesis of equal median in the distributions). Respectively, the median of $-\Delta_{RMSE,FFD}$ and the median of $-\Delta_{RMSE,ICP}$ were for L1 0.17 and 0.02, for L2 0.32 and 0.03, for L3 0.36 and 0.04, for L4 0.41 and 0.04, for L5 0.52 and 0.05, for L6 0.50 and 0.05. So, the results highlight the need to treat the intra-operative deformation with deformable registration algorithm to achieve a good registration accuracy. The absence of statistically significant differences (Wilcoxon test with $\alpha = 0.05$) between the values of $-\Delta_{RMSE}$ for L1 and $-\Delta_{RMSE}$ for L2 and $-\Delta_{RMSE}$ for L3 and so on highlights the robustness of FFD to tackle different levels of deformation, so the possibility to deal all the deformation occurring in the OR.

The inability of ICP to treat also the smallest deformation level is interesting: the smallest deformation can be considered the ideal situation in a partial nephrectomy, given all the possible intra-operative deformation sources. So, this fact highlights the need to continue the investigation of deformable registration algorithm in order to use it in partial nephrectomy AR system.

The same considerations can be done in the 3D case (*E4*), where the median of $-\Delta_{RMSE,FFD}$ and the median of $-\Delta_{RMSE,ICP}$ were, respectively 0.059 and 0.004 for L1, 0.054 and 0.005 for L2, 0.071 and 0.006 for L3, 0.064 and 0.007 for L4, 0.058 and 0.012 for L5, 0.080 and 0.009 for L6. The absence of statistically significant differences (Wilcoxon test with $\alpha = 0.05$) between the values of $-\Delta_{RMSE}$ for L1 and

$-\Delta_{RMSE}$ for L2 and $-\Delta_{RMSE}$ for L3 and so on was highlighted also here. So, the FFD algorithm showed also in 3D the ability to treat different levels of deformations in different locations of the intra-operative point cloud.

The complete workflow was used to register the two available pre-operative model $M1$ and $M2$ to the point cloud acquired with the phantom ($F2$).

The results of the Tab. 4.3 and 4.4 show that the developed workflow was able to tackle the deformable registration of the kidney models on the real point cloud. The final $RMSE_{registration}$ was strongly affected by the results of the manual alignment ($RMSE_{alignment}$). Indeed, the mean results of the deformable registration ($-\Delta_{RMSE,deformableregistration}$) was 0.11, however the highest values were obtained when the registration was performed on well aligned point cloud. The alignment was easier to be performed when only a small portion of the pre-operative volume was considered. The alignement, both manual or based landmark, was strongly affected by the user experience. By the way, the results are promising for the use of FFD deformable registration algorithm in a real scenario.

The proposed workflow deals only with the registration of the pre-operative model and the intra-operative point cloud, so the maintenance of the registration during the procedure is not handled. Regarding the proposed registration workflow, one of the main limitations is in the initial registration step: it is time consuming, strongly depends on the user and affects the entire workflow. Moreover, the registration adjustment step is based on the hypothesis that a wide portion of the surface is available: this does not always happens in the OR. The most time consuming phases in the current workflow are the segmentation of the pre-operative CT to retrieve the model and the segmentation of the intra-operative endoscopic view to retrieve the kidney surface. Moreover, currently the deformation is tackled only on the kidney surface, disregarding the volumetric information. Those issues have to be solved to obtain a more complete workflow.

Chapter 6

CONCLUSIONS AND FUTURE WORK

The workflow for deformable registration of the kidney model to the intra-operative point cloud is proposed. The registration is split in two phases: (i) the initial alignment, performed manually or based on corresponding landmark, and (ii) the deformable registration adjustment, performed with FFD algorithm based on B-splines.

The presented workflow obtained good registration results when it registered the entire kidney volume. However, there are still some issues that have to be solved.

First of all, the problem of the intra-operative tracking to maintain the registration is not treated. Some possible implementation of tracking are described in [13, 41]. The tracking issue can be addressed when the registration accuracy is high enough to justify the use of this technique to overcome the MIS drawback. As stated in [13], one open problem in every kind of AR system is to decide what to display to offer a real help to the surgeons.

Currently, the pre-operative kidney segmentation from CT to obtain an accurate patient-specific anatomical model is time consuming: it can be improved using automatic segmentation method for CT as in [61, 62, 63].

Another step to further automatize the registration procedure is the use of automatic intra-operative point cloud segmentation for the kidney surface recognition [64].

Regarding the registration workflow, currently the deformable registration adjustment relies on wide intra-operative kidney visible surface. Indeed, in [31] the feasibility of the image guided kidney surgery is studied and the it is stated that approximately 28% of the total surface is required to obtain a feasible augmentation. The currently partial nephrectomy procedure does not allow to retrieve such a wide point cloud, so other data should be exploited to allow an accurate registration.

Finally, the developed workflow can be integrated with a robotic system for the AC implementation. The AC are usually structures internal to the kidney (e.g. vessels and nerves); to identify them in the intra-operative scene starting from the pre-operative information, determine the kidney model surface deformation is not sufficient. Thus, a mass-spring-damper model can be developed to simulate the kidney volume deformation.

List of abbreviations

RCC: Renal Cell Cancer

CT: Computed Tomography

MRI: Magnetic Resonance Imaging

MIS: Minimal Invasive Surgery

RMIS: Robotic MIS

IGS: Image Guided Surgery

OR: Operating Room

AR: Augmented Reality

AC: Active-Constraints

US: Ultra Sounds

FFD: Free Form Deformation

dVRK: da Vinci Research Kit

VF: Vector Field

FMM: Fast Marching Method

$\vec{m} \in M$: surface model vertex

$\vec{f} \in F$: point of the intra-operative point cloud

$\vec{p} \in P$: pre-operative marker

$\vec{i} \in I$: intra-operative marker

d: distance

$\phi_{i,j,k} \in \Phi$: control point

n_x, n_y, n_z: number of control points in x, y, z dimension

$\delta_x, \delta_y, \delta_z$: spacing along x, y, z

dim_x, dim_y, dim_z: point cloud dimension along x, y, z

$T(x, y, z)$: transformation

$B_l(u), B_m(v), B_n(w)$: spline basis function

IEO: Istituto Europeo di Oncologia

VTK: Visualization Toolkit

ITK: Insight Segmentation and Registration Toolkit

$M1$: kidney model from Ircadb2

$M2$: kidney model from IEO

$F1$: manually deformed point cloud

$F2$: point cloud acquired on silicon phantom

$-\Delta_{RMSE}$: error reduction

$RMSE$: Root Mean Squared Error

E: experiment

$iter_{max}$: maximum number of iteration

Y: correspondence relation between points

$\vec{q_R}$: rotation expressed in quaternion

$\vec{q_T}$: translation expressed in quaternion

List of figures

FIGURE 1.1 Estimated cancer incidence worldwide in 2012 according to WHO. 1

FIGURE 1.2 Kidney cancer in computed tomography. 2

FIGURE 1.3 Ports comparison in open (left) and laparoscopic surgery (right). 3

FIGURE 1.4 Set-up in laparoscopic nephrectomy. 4

FIGURE 1.5 Augmented reality in surgery. On the intra-operative scene organs model are projected (central). The endoscopic view is displayed without augmentation (left) and with augmentation (right). 5

FIGURE 1.6 Augmented reality in neurosurgery. 7

FIGURE 1.7 Augmented reality in nephrectomy: superimposition of the intra-operative anatomy to the intra-operative scene. From [30]. 8

FIGURE 1.8 From [40]. 2D tumor boundaries extracted from pre-operative CT are projected onto the intra-operative endoscopic images. Each contour has associated a probability. 10

FIGURE 2.1 The registration workflow to register the moving point cloud to the reference point cloud. A metric based on distance is set between the two point clouds. The metric is optimized for finding the best parameters to be used in the transformation (i.e. the mathematical operators that maps one dataset into another one). The transformation is applied to the moving point cloud. This process is iteratively done until convergence in terms of metric reduction is reached. 14

FIGURE 2.2 The Vector Field (VF) is a possible transformation involved in registration. VF is a grid superimposed to the point cloud, in which each block has associated a displacement vector, representing the direction and the intensity applied to what is inside that block. 16

FIGURE 2.3 The point-based approach: the registration is performed between markers (black dots) from the model (gray) and markers from the intra-operative endoscopic image (red). The result is from [31]. 17

FIGURE 2.4 The surface-based approach: the registration is performed between the pre-operative or intra-operative model surface (gray surface) and intra-operative surface (red surface). The resulting view is from [31]. 18

FIGURE 2.5 The volume-based approach: the registration is performed between the pre-operative or intra-operative model volume (yellow) and intra-operative volume (green). 20

FIGURE 3.1 The proposed registration workflow for augmented reality in nephrectomy. 23

FIGURE 3.2 The steps of the model generation: (left) segmentation of the computed tomography with active contours model; (center) kidney model obtained with fast marching method; (right) retrieved model vertexes (M). 24

FIGURE 3.3 The steps of the 3D reconstruction: (left) stereoimages acquired with the da Vinci Research Kit endoscope; (right) intra-operative point cloud retrieved with the dense soft-tissue 3D reconstruction. 25

FIGURE 3.4 The manual alignment was performed with the Slicer interface. The rotations angles and the values of translations were manually set. . 26

FIGURE 3.5 Point-based registration of the kidney model to the intra-operative point cloud. (Left) From the kidney model vertexes ($\vec{p} \in P$, blue dots) and the intra-operative point cloud ($\vec{i} \in I$, pink dots), corresponding markers (green dots) were identified. (Right) The point-based registration was computed and the transformation was applied. 26

FIGURE 3.6 The deformation of the control points ($\phi_{i,j}$) mesh Φ in Free Form Deformation model in 2D. (Left) Φ is built over the moving point cloud (blue dots). A cost function based on the distance between the moving point cloud and the fixed one (red stars) is minimized and the $\phi_{i,j}$ displacement is computed (the $\phi_{0,4}$ displacement in shown in green). (Right) the transformation retrieved is applied to all the moving points. 28

FIGURE 3.7 The silicon kidney phantom obtained according to the pre-operative model. 29

FIGURE 3.8 (Left) 3D model point cloud; (right) model point cloud in 2D obtained retrieving the 2D boundaries of the 3D model projected on a plane. 30

FIGURE 3.9 (Left) kidney model; (right) kidney model deformed with the open source 3D creation suite Blender to test the registration in a controlled environment. 31

FIGURE 3.10 The 2D intra-operative point clouds ($F1$) manually obtained from the 2D kidney model boundary. Starting from ten different positions on the model cloud, the deformation is progressively increased from L1 (the smallest) to L6 (the biggest). 31

FIGURE 4.1 Experiment *E2* results. $-\Delta_{RMSE}$ was the Root Mean Square Error (RMSE) reduction and $iter_{max}$ was the maximum number of iteration. The results were obtained registering in 2D with Free Form Deformation algorithm the model boundary to ten manually deformed boundary with medium deformation level. 38

FIGURE 4.2 Experiment E3 results. On the horizontal axis are reported the deformation levels (L) of the manually deformed boundary (the intra-operative point cloud to which the model boundary was registered). The $-\Delta_{RMSE,ICP}$ was the Root Mean Square Error (RMSE) reduction of Iterative Closest Point (ICP) algorithm (orange). The $-\Delta_{RMSE,FFD}$ was the RMSE reduction of Free Form Deformation (FFD) algorithm (blue). Statistical significant difference (given by Wilcoxon test with p $< \alpha$) are represented with a star. 39

FIGURE 4.3 Experiment E3 results. $-\Delta_{RMSE,ICP}$ (a) was the Root Mean Square Error (RMSE) reduction for Iterative Closest Point (ICP) registration algorithm and $-\Delta_{RMSE,FFD}$ (b) was the RMSE reduction for FFD algorithm. On the horizontal axis the deformation levels (L) of the manually deformed boundary to which the model boundary was registered are represented. The absence of significant difference is represented with black lines. 40

FIGURE 4.4 An example of deformable registration results from experiment E3. (Left) Initial situation: the blue point cloud was the pre-operative model boundary and the pink point cloud was the manually deformed point cloud. (Right) After deformable registration. 40

FIGURE 4.5 Experiment E4 results. On the horizontal axis are reported the deformation levels (L) of the manually deformed boundary (the intra-operative point cloud to which the model boundary was registered). The $-\Delta_{RMSE,ICP}$ was the ROot Mean Square Error (RMSE) reduction of Iterative Closest Point (ICP) algorithm (orange). The $-\Delta_{RMSE,FFD}$ was the RSME reduction of Free Form Deformation (FFD) algorithm (blue). Statistical significant difference (given by Wilcoxon test with p $< \alpha$) are represented with a star. 41

FIGURE 4.6 Experiment E4 results. $-\Delta_{RMSE,ICP}$ (a) was the Root Mean Square Error (RMSE) reduction for Iterative Closest Point (ICP) registration algorithm and $-\Delta_{RMSE,FFD}$ (b) was the RMSE reduction for FFD algorithm. On the horizontal axis the deformation levels (L) of the manually deformed boundary to which the model boundary was registered are represented. The absence of significant difference is represented with black lines, while the presence of significant difference is represented with red lines. 42

FIGURE 4.7 Experiment E5 results obtained with the entire kidney model. (Left) Initial situation: the blue point cloud was the pre-operative model and the pink point cloud was the intra-operative surface acquired on kidney phantom. (Center) The alignment was performed manually. (Right) After deformable registration. 43

FIGURE 4.8 Experiment E5 results obtained with part of the kidney model. (Left) Initial situation: the blue point cloud was the pre-operative model and the pink point cloud was the intra-operative surface acquired on kidney phantom. (Center) The alignment was performed manually. (Right) After deformable registration. 44

FIGURE 4.9 Experiment E6 results obtained with the entire kidney model. (Left) Initial situation: the blue point cloud was the pre-operative model and the pink point cloud was the intra-operative surface acquired on kidney phantom. (Center) The alignment was performed manually. (Right) After deformable registration. 44

FIGURE 4.10 Experiment E6 results obtained with part of the kidney model. (Left) Initial situation: the blue point cloud was the pre-operative model and the pink point cloud was the intra-operative surface acquired on kidney phantom. (Center) The alignment was performed manually. (Right) After deformable registration. 45

FIGURE 4.11 Experiment E7 results obtained with the entire kidney model. (Left) Initial situation: the blue point cloud was the pre-operative model and the pink point cloud was the intra-operative surface acquired on kidney phantom. (Center) The alignment was performed with markers. (Right) After deformable registration. 45
FIGURE 4.12 Experiment E7 results obtained with part of the kidney model. (Left) Initial situation: the blue point cloud was the pre-operative model and the pink point cloud was the intra-operative surface acquired on kidney phantom. (Center) The alignment was performed with markers. (Right) After deformable registration. 46
FIGURE 4.13 Experiment E8 results obtained with the entire kidney model. (Left) Initial situation: the blue point cloud was the pre-operative model and the pink point cloud was the intra-operative surface acquired on kidney phantom. (Center) The alignment was performed with markers. (Right) After deformable registration. 46
FIGURE 4.14 Experiment E8 results obtained with part of the kidney model. (Left) Initial situation: the blue point cloud was the pre-operative model and the pink point cloud was the intra-operative surface acquired on kidney phantom. (Center) The alignment was performed with markers. (Right) After deformable registration. 47

List of tables

TABLE 3.1 $M1$ was the model vertexes point cloud obtained from the Ircadb Computed Tomography (CT) with manual segmentation and Fast Marching Method (FFM) reconstruction. $M2$ was the model vertexes point cloud obtained segmenting (deformable model active contours) and reconstructing (FFM) an abdominal CT from the Istituto Europeo di Oncologia. $F1$ was the intra-operative point cloud obtained manually deforming $M1$ with Blender, an open source software. $F2$ was the intra-operative point cloud retrieved from the da Vinci Reseach Kit's endoscopic acquisitions on kidney silicon phantom (dense soft-tissue 3D reconstruction). FFD was the Free Form Deformation registration algorithm, based on a mesh grid whose control points are separated by spacing δ. ICP was the Iterative Closest Point rigid registration algorithm. $iter_{max}$ is the maximum number of iteration of the registration algorithm. $-\Delta_{RMSE}$ is the Root Mean Square Error (RMSE) reduction. 36

TABLE 4.1 Expetiment E1 results. n_x and n_y were the number of control points along the x and y direction, respectively. Δ_{RMSE} was the Root Mean Square Error (RMSE) reduction. dim_x and dim_y were the reference point cloud dimensions along x and y. 38

TABLE 4.2 Relation between the maximum number of iteration ($iter_{max}$) and the computational time in Free Form Deformable registration algorithm for *E2*. The mean computational time was computed on the registration of the 2D model boundary to ten manually deformed kidney boundary with medium deformation level. 39

TABLE 4.3 Epxeriments E5, E6, E7, E8 results. $RMSE_{before}$ was the Root Mean Square Error (RMSE) before the registration, $RMSE_{alignment}$ was the RMSE after the alignment, used to initialize the registration, and $RMSE_{registration}$ was the RMSE after the deformable registration. The experiments protocol are reported in Tab. 3.1. $M1$ was the model obtained from the Irbadb2 Computed Tomography (CT) with manual segmentation and Fast Marching Method (FMM) reconstruction, $M2$ was the model obtained from CT from Istituto Europeo di Oncologia with deformable model active contour segmentation and FMM reconstruction. 42

TABLE 4.4 Experiments E5, E6, E7, E8 results. $-\Delta_{RMSE,initialalignment}$ was the Root Mean Square Error (RMSE) reduction in the initial alignment, performed according to the experimental protocol, and $-\Delta_{RMSE,deformableregistration}$ was the RMSE reduction in the deformable registration. The experiments protocol are reported in Tab. 3.1. $M1$ was the model obtained from the Irbadb2 Computed Tomography (CT) with manual segmentation and Fast Marching Method (FMM) reconstruction, $M2$ was the model obtained from CT from Istituto Europeo di Oncologia with deformable model active contour segmentation and FMM reconstruction. 43

Bibliography

[1] M. Crundwell, "Pathology and genetics of tumours of the urinary system and male genital organs," *Bju International*, vol. 94, no. 4, pp. 675–675, 2004.

[2] A. Schneider, S. Pezold, A. Sauer, J. Ebbing, S. Wyler, R. Rosenthal, and P. C. Cattin, "Augmented reality assisted laparoscopic partial nephrectomy," in *International Conference on Medical Image Computing and Computer-Assisted Intervention*, pp. 357–364, Springer, 2014.

[3] T. M. Fullum, J. A. Ladapo, B. J. Borah, and C. L. Gunnarsson, "Comparison of the clinical and economic outcomes between open and minimally invasive appendectomy and colectomy: evidence from a large commercial payer database," *Surgical Endoscopy*, vol. 24, no. 4, pp. 845–853, 2010.

[4] H. Himal, "Minimally invasive (laparoscopic) surgery," *Surgical Endoscopy And Other Interventional Techniques*, vol. 16, no. 12, pp. 1647–1652, 2002.

[5] Y. S. Kwoh, J. Hou, E. A. Jonckheere, and S. Hayati, "A robot with improved absolute positioning accuracy for ct guided stereotactic brain surgery," *IEEE Transactions on Biomedical Engineering*, vol. 35, no. 2, pp. 153–160, 1988.

[6] C. Giorgi, H. Eisenberg, G. Costi, E. Gallo, G. Garibotto, and D. S. Casolino, "Robot-assisted microscope for neurosurgery," *Journal of image guided surgery*, vol. 1, no. 3, pp. 158–163, 1995.

[7] M. Chen, T. Wang, Q. Zhang, Y. Zhang, and Z. Tian, "A robotics system for stereotactic neurosurgery and its clinical application," in *Robotics and Automation, 1998. Proceedings. 1998 IEEE International Conference on*, vol. 2, pp. 995–1000, IEEE, 1998.

[8] S. Nicolau, L. Soler, D. Mutter, and J. Marescaux, "Augmented reality in laparoscopic surgical oncology," *Surgical oncology*, vol. 20, no. 3, pp. 189–201, 2011.

[9] A. Hinsche and R. Smith, "Image-guided surgery," *Current orthopaedics*, vol. 15, no. 4, pp. 296–303, 2001.

[10] H. O. Altamar, R. E. Ong, C. L. Glisson, D. P. Viprakasit, M. I. Miga, S. D. Herrell, and R. L. Galloway, "Kidney deformation and intraprocedural registration: a study of elements of image-guided kidney surgery," *Journal of endourology*, vol. 25, no. 3, pp. 511–517, 2011.

[11] D. Yu, J. S. Jin, S. Luo, W. Lai, and Q. Huang, "A useful visualization technique: a literature review for augmented reality and its application, limitation & future direction," in *Visual information communication*, pp. 311–337, Springer, 2009.

[12] S. Moccia, E. De Momi, S. El Hadji, and L. S. Mattos, "Blood vessel segmentation algorithms–Review of methods, datasets and evaluation metrics," *Computer Methods and Programs in Biomedicine*, vol. 158, pp. 71–91, 2018.

[13] S. Bernhardt, S. A. Nicolau, L. Soler, and C. Doignon, "The status of augmented reality in laparoscopic surgery as of 2016," *Medical image analysis*, vol. 37, pp. 66–90, 2017.

[14] A. Hughes-Hallett, E. K. Mayer, H. J. Marcus, T. P. Cundy, P. J. Pratt, A. W. Darzi, and J. A. Vale, "Augmented reality partial nephrectomy: examining the current status and future perspectives," *Urology*, vol. 83, no. 2, pp. 266–273, 2014.

[15] S. E. Sutherland, M. I. Resnick, G. T. Maclennan, and H. B. Goldman, "Does the size of the surgical margin in partial nephrectomy for renal cell cancer really matter?," *The Journal of urology*, vol. 167, no. 1, pp. 61–64, 2002.

[16] J. S. Lam, J. Bergman, A. Breda, and P. G. Schulam, "Importance of surgical margins in the management of renal cell carcinoma," *Nature clinical practice Urology*, vol. 5, no. 6, pp. 308–317, 2008.

[17] D. W. Roberts, J. W. Strohbehn, J. F. Hatch, W. Murray, and H. Kettenberger, "A frameless stereotaxic integration of computerized tomographic imaging and the operating microscope," *Journal of neurosurgery*, vol. 65, no. 4, pp. 545–549, 1986.

[18] P. J. Kelly, B. A. Kall, S. Goerss, and F. Earnest IV, "Computer-assisted stereotaxic laser resection of intra-axial brain neoplasms," *Journal of neurosurgery*, vol. 64, no. 3, pp. 427–439, 1986.

[19] R. Sawaya, W. M. Rambo Jr, M. A. Hammoud, and B. L. Ligon, "Advances in surgery for brain tumors.," *Neurologic clinics*, vol. 13, no. 4, pp. 757–771, 1995.

[20] I. Cabrilo, K. Schaller, and P. Bijlenga, "Augmented reality-assisted bypass surgery: embracing minimal invasiveness," *World neurosurgery*, vol. 83, no. 4, pp. 596–602, 2015.

[21] F. Sauer, A. Khamene, B. Bascle, and G. J. Rubino, "A head-mounted display system for augmented reality image guidance: Towards clinical evaluation for imri-guided neurosurgery," in *Proceedings of the 4th International Conference on Medical Image Computing and Computer-Assisted Intervention*, pp. 707–716, Springer-Verlag, 2001.

[22] W. Lorensen, H. Cline, C. Nafis, R. Kikinis, D. Altobelli, and L. Gleason, "Enhancing reality in the operating room," in *Visualization, 1993. Visualization'93, Proceedings., IEEE Conference on*, pp. 410–415, IEEE, 1993.

[23] W. E. L. Grimson, G. J. Ettinger, S. J. White, P. L. Gleason, T. Lozano-Pérez, W. Wells, and R. Kikinis, "Evaluating and validating an automated registration system for enhanced reality visualization in surgery," in *Computer Vision, Virtual Reality and Robotics in Medicine*, pp. 3–12, Springer, 1995.

[24] M. Bajura, H. Fuchs, and R. Ohbuchi, "Merging virtual objects with the real world: Seeing ultrasound imagery within the patient," in *ACM SIGGRAPH Computer Graphics*, vol. 26, pp. 203–210, ACM, 1992.

[25] J. Marescaux, F. Rubino, M. Arenas, D. Mutter, and L. Soler, "Augmented-reality–assisted laparoscopic adrenalectomy," *Jama*, vol. 292, no. 18, pp. 2211–2215, 2004.

[26] E. Marzano, T. Piardi, L. Soler, M. Diana, D. Mutter, J. Marescaux, and P. Pessaux, "Augmented reality-guided artery-first pancreatico-duodenectomy," *Journal of Gastrointestinal Surgery*, vol. 17, no. 11, pp. 1980–1983, 2013.

[27] P. Pessaux, M. Diana, L. Soler, T. Piardi, D. Mutter, and J. Marescaux, "Towards cybernetic surgery: robotic and augmented reality-assisted liver segmentectomy," *Langenbeck's archives of surgery*, vol. 400, no. 3, pp. 381–385, 2015.

[28] K. Konishi, M. Hashizume, M. Nakamoto, Y. Kakeji, I. Yoshino, A. Taketomi, Y. Sato, S. Tamura, and Y. Maehara, "Augmented reality navigation system for endoscopic surgery based on three-dimensional ultrasound and computed tomography: Application to 20 clinical cases," in *International Congress Series*, vol. 1281, pp. 537–542, Elsevier, 2005.

[29] O. Ukimura and I. S. Gill, "Imaging-assisted endoscopic surgery: Cleveland clinic experience," *Journal of Endourology*, vol. 22, no. 4, pp. 803–810, 2008.

[30] D. Teber, S. Guven, T. Simpfendörfer, M. Baumhauer, E. O. Güven, F. Yencilek, A. S. Gözen, and J. Rassweiler, "Augmented reality: a new tool to improve surgical accuracy during laparoscopic partial nephrectomy? preliminary in vitro and in vivo results," *European urology*, vol. 56, no. 2, pp. 332–338, 2009.

[31] A. B. Benincasa, L. W. Clements, S. D. Herrell, and R. L. Galloway, "Feasibility study for image-guided kidney surgery: Assessment of required intraoperative surface for accurate physical to image space registrations," *Medical physics*, vol. 35, no. 9, pp. 4251–4261, 2008.

[32] C. Glisson, R. Ong, A. Simpson, P. Clark, S. D. Herrell, and R. Galloway, "The use of virtual fiducials in image-guided kidney surgery," in *Medical Imaging 2011: Visualization, Image-Guided Procedures, and Modeling*, vol. 7964, p. 796402, International Society for Optics and Photonics, 2011.

[33] L.-M. Su, B. P. Vagvolgyi, R. Agarwal, C. E. Reiley, R. H. Taylor, and G. D. Hager, "Augmented reality during robot-assisted laparoscopic partial nephrectomy: toward real-time 3d-ct to stereoscopic video registration," *Urology*, vol. 73, no. 4, pp. 896–900, 2009.

[34] P. Pratt, E. Mayer, J. Vale, D. Cohen, E. Edwards, A. Darzi, and G.-Z. Yang, "An effective visualisation and registration system for image-guided robotic partial nephrectomy," *Journal of Robotic Surgery*, vol. 6, no. 1, pp. 23–31, 2012.

[35] A. Hughes-Hallett, P. Pratt, E. Mayer, A. Di Marco, G.-Z. Yang, J. Vale, and A. Darzi, "Intraoperative ultrasound overlay in robot-assisted partial nephrectomy: first clinical experience," *European urology*, vol. 65, no. 3, pp. 671–672, 2014.

[36] K. Nakamura, Y. Naya, S. Zenbutsu, K. Araki, S. Cho, S. Ohta, N. Nihei, H. Suzuki, T. Ichikawa, and T. Igarashi, "Surgical navigation using three-dimensional computed tomography images fused intraoperatively with live video," *Journal of endourology*, vol. 24, no. 4, pp. 521–524, 2010.

[37] C. L. Cheung, C. Wedlake, J. Moore, S. E. Pautler, A. Ahmad, and T. M. Peters, "Fusion of stereoscopic video and laparoscopic ultrasound for minimally invasive partial nephrectomy," in *Medical Imaging 2009: Visualization, Image-Guided Procedures, and Modeling*, vol. 7261, p. 726109, International Society for Optics and Photonics, 2009.

[38] M. Baumhauer, T. Simpfendörfer, B. P. Müller-Stich, D. Teber, C. N. Gutt, J. Rassweiler, H.-P. Meinzer, and I. Wolf, "Soft tissue navigation for laparoscopic partial nephrectomy," *International Journal of Computer Assisted Radiology and Surgery*, vol. 3, no. 3-4, p. 307, 2008.

[39] R. E. Ong, S. D. Herrell, M. I. Miga, and R. L. Galloway, "A kidney deformation model for use in non-rigid registration during image-guided surgery," in *Medical Imaging 2008: Visualization, Image-Guided Procedures, and Modeling*, vol. 6918, p. 69180W, International Society for Optics and Photonics, 2008.

[40] A. Amir-Khalili, M. S. Nosrati, J.-M. Peyrat, G. Hamarneh, and R. Abugharbieh, "Uncertainty-encoded augmented reality for robot-assisted partial nephrectomy: A phantom study," in *Augmented Reality Environments for Medical Imaging and Computer-Assisted Interventions*, pp. 182–191, Springer, 2013.

[41] M. C. Yip, D. G. Lowe, S. E. Salcudean, R. N. Rohling, and C. Y. Nguan, "Tissue tracking and registration for image-guided surgery," *IEEE transactions on medical imaging*, vol. 31, no. 11, pp. 2169–2182, 2012.

[42] M. Sonka, J. M. Fitzpatrick, and B. R. Masters, "Handbook of medical imaging, volume 2: Medical image processing and analysis," *Optics & Photonics News*, vol. 13, pp. 50–51, 2002.

[43] P. J. Besl, N. D. McKay, *et al.*, "A method for registration of 3-d shapes," *IEEE Transactions on pattern analysis and machine intelligence*, vol. 14, no. 2, pp. 239–256, 1992.

[44] Z. Zhang, "Iterative point matching for registration of free-form curves and surfaces," *International journal of computer vision*, vol. 13, no. 2, pp. 119–152, 1994.

[45] A. Sotiras, C. Davatzikos, and N. Paragios, "Deformable medical image registration: A survey," *IEEE transactions on medical imaging*, vol. 32, no. 7, pp. 1153–1190, 2013.

[46] T. W. Sederberg and S. R. Parry, "Free-form deformation of solid geometric models," *ACM SIGGRAPH computer graphics*, vol. 20, no. 4, pp. 151–160, 1986.

[47] D. Rueckert, L. I. Sonoda, C. Hayes, D. L. Hill, M. O. Leach, and D. J. Hawkes, "Non-rigid registration using free-form deformations: application to breast mr images," *IEEE transactions on medical imaging*, vol. 18, no. 8, pp. 712–721, 1999.

[48] B. Marques, R. Plantefeve, F. Roy, N. Haouchine, E. Jeanvoine, I. Peterlik, and S. Cotin, "Framework for augmented reality in minimally invasive laparoscopic surgery," in *E-health Networking, Application & Services (HealthCom), 2015 17th International Conference on*, pp. 22–27, IEEE, 2015.

[49] L. Maier-Hein, P. Mountney, A. Bartoli, H. Elhawary, D. Elson, A. Groch, A. Kolb, M. Rodrigues, J. Sorger, S. Speidel, *et al.*, "Optical techniques for 3d surface reconstruction in computer-assisted laparoscopic surgery," *Medical image analysis*, vol. 17, no. 8, pp. 974–996, 2013.

[50] Y. Gao, R. Kikinis, S. Bouix, M. Shenton, and A. Tannenbaum, "A 3d interactive multi-object segmentation tool using local robust statistics driven active contours," *Medical image analysis*, vol. 16, no. 6, pp. 1216–1227, 2012.

[51] M. Kass, A. Witkin, and D. Terzopoulos, "Snakes: Active contour models," *International journal of computer vision*, vol. 1, no. 4, pp. 321–331, 1988.

[52] J. A. Sethian, "Fast marching methods," *SIAM review*, vol. 41, no. 2, pp. 199–235, 1999.

[53] Z. Zhang, "A flexible new technique for camera calibration," *IEEE Transactions on pattern analysis and machine intelligence*, vol. 22, no. 11, pp. 1330–1334, 2000.

[54] V. Penza, J. Ortiz, L. S. Mattos, A. Forgione, and E. De Momi, "Dense soft tissue 3d reconstruction refined with super-pixel segmentation for robotic abdominal surgery," *International journal of computer assisted radiology and surgery*, vol. 11, no. 2, pp. 197–206, 2016.

[55] D. Khodadad, A. Ahmadian, M. Ay, A. F. Esfahani, H. Y. Banaem, and H. Zaidi, "B-spline based free form deformation thoracic non-rigid registration of ct and pet images," in *International Conference on Graphic and Image Processing (ICGIP 2011)*, vol. 8285, p. 82851K, International Society for Optics and Photonics, 2011.

[56] S. Kabus, T. Netsch, B. Fischer, and J. Modersitzki, "B-spline registration of 3d images with levenberg-marquardt optimization," in *Medical Imaging 2004: Image Processing*, vol. 5370, pp. 304–314, International Society for Optics and Photonics, 2004.

[57] D. Mattes, D. R. Haynor, H. Vesselle, T. K. Lewellen, and W. Eubank, "Pet-ct image registration in the chest using free-form deformations," *IEEE transactions on medical imaging*, vol. 22, no. 1, pp. 120–128, 2003.

[58] D. W. Marquardt, "An algorithm for least-squares estimation of nonlinear parameters," *Journal of the society for Industrial and Applied Mathematics*, vol. 11, no. 2, pp. 431–441, 1963.

[59] K. Levenberg, "A method for the solution of certain non-linear problems in least squares," *Quarterly of applied mathematics*, vol. 2, no. 2, pp. 164–168, 1944.

[60] S. Condino, M. Carbone, V. Ferrari, L. Faggioni, A. Peri, M. Ferrari, and F. Mosca, "How to build patient-specific synthetic abdominal anatomies. an innovative approach from physical toward hybrid surgical simulators," *The International Journal of Medical Robotics and Computer Assisted Surgery*, vol. 7, no. 2, pp. 202–213, 2011.

[61] G. Yan and B. Wang, "An automatic kidney segmentation from abdominal ct images," in *Intelligent Computing and Intelligent Systems (ICIS), 2010 IEEE International Conference on*, vol. 1, pp. 280–284, IEEE, 2010.

[62] C.-C. Lee, P.-C. Chung, and H.-M. Tsai, "Identifying multiple abdominal organs from ct image series using a multimodule contextual neural network and spatial fuzzy rules," *IEEE Transactions on Information Technology in Biomedicine*, vol. 7, no. 3, pp. 208–217, 2003.

[63] D.-T. Lin, C.-C. Lei, and S.-W. Hung, "Computer-aided kidney segmentation on abdominal ct images," *IEEE transactions on information technology in biomedicine*, vol. 10, no. 1, pp. 59–65, 2006.

[64] S. Moccia, S. J. Wirkert, H. Kenngott, A. S. Vemuri, M. Apitz, B. Mayer, E. De Momi, L. S. Mattos, and L. Maier-Hein, "Uncertainty-aware organ classification for surgical data science applications in laparoscopy," *arXiv preprint arXiv:1706.07002*, 2017.